2020-08-01

Interfacial response of fibre-to-matrix in textile reinforced concrete between two cracks: Analytical solution

Cheng, S

10.1016/j.compstruct.2020.112380
Composite Structures
Elsevier

Interfacial response of fibre-to-matrix in textile reinforced concrete between two cracks: analytical solution

Shanshan Cheng, Jie Ji, Maozhou Meng*
School of Engineering, Computing and Mathematics (SECAM), University of Plymouth, UK. PL4 8AA
E-mail: Maozhou.meng@plymouth.ac.uk

Abstract:
Textile reinforced concrete (TRC) has been increasingly used in strengthening existing structures and building new lightweight structures, and the interfacial bond plays a fundamental role in optimising the structural performance and design. This paper, for the first time, presents an analytical solution to predict the interfacial response of a textile reinforced concrete composite between two cracks. The closed form expressions not only apply to predict pull-out force vs. displacement relation, but also simulate interfacial response between two locations. The interfacial behaviour, including the interfacial relative slip, the shear stress distribution, and the axial stresses of the reinforcement and the matrix, could be obtained. While the numerical parametric studies are based on carbon fibre textile reinforced concrete, the theoretical solutions are applicable to other embedded type reinforced composites. The accuracy of the derived theoretical model has been validated using previously published researches of similar problems and the FEM simulation. The numerical parametric studies concluded that increasing the load difference at the two ends of the reinforcement (increasing β value) may shift the critical failure mode from interfacial debonding to material yielding. Furthermore, using micro/short fibres in the concrete matrix (triggering a negative η value) will significantly improve the interfacial performance. It is also found that for a concrete composite with a high reinforcement ratio, it is necessary to use either ultra-high strength concrete or fibre reinforced concrete matrix to fully use the high tensile strength capacity of carbon fibres.

Keywords: bond-slip; interface; analytical solution; textile reinforced concrete.

1. Introduction

In recent years, fibre-reinforced polymer (FRP) materials have become widely used in reinforced concrete in place of conventional steel reinforcement for their advantages such as high strength, light weight and great corrosion resistance in marine environment [1-3]. Conventionally FRP has been produced in bar shapes to imitate the steel rebar. However, the application has been held back due to difficulties in bending the FRP bars at the connections. In contrast, textile fabrics made of fibre bundles have offset those limitations. Therefore, textile reinforced concrete (TRC), using high strength fine aggregated concrete matrix and multi-axial corrosion-resistant textile mesh, has been extensively researched over the past decade [4]. Although it is more attractive to newly built slender, lightweight and flexible structures [5], attention has been seen on strengthening existing structures [6, 7]. A RILEM report [8] has reviewed recent research and provided guidelines for future design and testing.

Bonding is one of the key mechanical properties of textile reinforced concrete. Like conventional reinforced concrete structures, cracks develop in the tension zone of the concrete due to its low resistance to tensile stress. Cracks begin to develop when the concrete reaches the ultimate tensile strength, whilst before then the textile reinforced concrete behaviour mainly depends on modulus of elasticity of the concrete due to the small reinforcement ratio (less than

3%). However, at the cracked section, the load is completely carried by the reinforcement. Multiple cracks can only form when there is enough bonding between fibre and the matrix and sufficient stiffness of the reinforcement to prevent cracks from widening [9]. Sufficient and fine cracks develop due to efficient transfer of the stress from fibre to concrete. Therefore, an increase in the number of cracks indicates an improvement in the bond.

The interfacial behaviour of textile reinforced concrete has attracted many researchers in the past decades. The most popular experimental method is the pull-out test, where fibre or strand is pulled out from the surrounding matrix, and the corresponding global load-displacement relation is recorded. Many tests have been carried out using this principle [10-15, 32-33, 36-39], although the experimental setup may be slightly different between tests [40]. A recent paper [39] has advanced this research by investigating the effect of different test setup on the interfacial response in TRC. In addition to experimental investigations, a variety of theoretical and numerical methods have been developed to evaluate the local interfacial properties through the pull-out test results. Conventionally it is assumed that the slip and bond shear stress are constant throughout the bond length [16]. This assumption has been widely accepted for carbon steel rebars, but its application to carbon fibre textiles is questionable due to the largely nonlinear distribution of the slip and interfacial shear stress along the bond length [17].

To date, many numerical methods, either based on optimization algorithms [19-22] or finite element method [19-20, 23], have been carried out. Although the numerical methods have become easier than ever with the modern computing technology, it is still computationally expensive, especially in conducting a large number of parametric studies [42]. While the analytical solutions are more difficult to obtain, they have unique advantages in assisting structural design as well as validation of numerical models. Various analytical or semi-analytical solutions [24-28] have been derived by far, all of which targeted at predicting the pull-out test results. In this paper, the analytical method has been taken one step further, to simulate the full-range interfacial behaviour of textile reinforced concrete between two cracks. The direct method is adopted, whereby given a local bond-slip relation, the global load-displacement relationship is derived. The novelty of this paper, compared with other similar researches [24-28, 36, 39], is that it not only enables simulation of pull-out tests, but also allows to predict interfacial responses and minimum crack spacing. The theoretical model was validated using a FEA model based on cohesive element method (CZM). Although the present model was developed for textile reinforced concrete, the formulae were derived in a general form. Therefore, it is also applicable to other types of fibre reinforced composites.

2. 1D analytical model

This paper presents a 1D analytical model for fibre-to-matrix bonded section between two locations (Figure 1(a)). Uniaxial forces are applied along the longitudinal direction. In a textile mesh, the warp and weft tows are usually independent from each other, where a stitch yarn ties the warp and weft tows to a required mesh type and mesh size [41]. Therefore, when the textile mesh is loaded in one direction, the transverse fibres are minimally stressed, which can be neglected in the idealised model. In a general case, the longitudinal fibre is subjected to different tensile forces at both ends, while the matrix is subjected to two axial forces, which could be tensile or compressive, at the two ends.

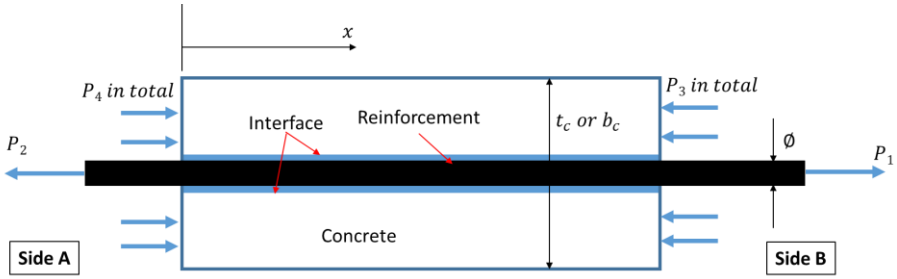

(a) Longitudinal view of idealised reinforced concrete model between two cracks

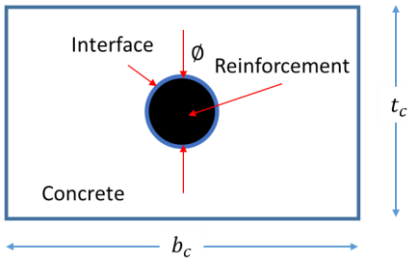

(b) Cross-sectional view of idealised reinforced concrete model between two cracks

Figure 1 Idealized model of fibre-to-concrete bonded interface

Figure 1 shows a schematic diagram of the fibre-to-matrix model. P_1 and P_2 are the tensile forces at each end of the fibre. Without losing generality, it is assumed that $P_1 \geq P_2 \geq 0$. The matrix is subjected to P_3 and P_4 at the two ends, which could be either tensile or compressive. It is also assumed that the forces remain proportional to each other throughout the loading process, i.e. the ratio among P_1, P_2, P_3 and P_4 remain constant during the debonding process. The width and thickness of matrix are b_c and t_c respectively. The fibre is assumed to be circular with constant section along the length, with a diameter of ϕ. The bonded length is denoted by L. The Young's modulus of the fibre and the matrix are E_p and E_c respectively. The adhesive layer is assumed to have a constant thickness.

Note that in such a model, the interface of the model is mainly subjected to shear deformations, which includes the actual adhesive layer, and those of a thin layer of adjacent concrete. Clearly, the failure mode of the interface is predominantly mode II interfacial fracture. It is assumed that the fibre and matrix are subjected to axial deformations only, while the interface is subjected to pure shear deformation only. Thus, all bending deformation is neglected, and the shear stress across the thickness of the interface is constant.

A horizontal coordinate system originating from the left end (side A in Figure 1(a)) is adopted. The differential equation expressing equilibrium conditions along the reinforcement can be defined as [24, 35]

$$A_p \frac{d\sigma_p}{dx} - \pi \phi \tau = 0 \quad (1)$$

$$A_p \sigma_p + A_c \sigma_c = P = P_1 - P_3 = P_2 - P_4 \quad (2)$$

where $A_p = \frac{\pi \phi^2}{4}$ is the cross-sectional area of the reinforcement, and $A_c = b_c t_c$ is the cross-sectional area of the matrix; σ_p and σ_c are the axial stress in the reinforcement and matrix respectively, and τ is the bond stress. Assuming both the reinforcement and matrix are in the elastic range throughout the loading process, the constitutive equations of the adhesive layer and the two adherends are

$$\tau = f(\delta) \quad (3)$$

$$\sigma_p = E_p \frac{du_p}{dx} \quad (4)$$

$$\sigma_c = E_c \frac{du_c}{dx} \quad (5)$$

The interfacial slip δ is defined as the relative displacement between the two adherends:

$$\delta = u_p - u_c \tag{6}$$

After substituting Eqs. (2-6) into Eq. (1), the governing equation is obtained:

$$\frac{d^2\delta}{dx^2} - \lambda^2\tau = 0 \tag{7}$$

where $\lambda^2 = \pi\emptyset\gamma$ and $\gamma = \frac{1}{E_pA_p} + \frac{1}{E_cA_c}$

The axial stresses in the reinforcement and concrete could be reformatted as follows:

$$\sigma_p = \frac{1}{A_p\gamma}\left(\frac{d\delta}{dx} + \frac{P}{E_cA_c}\right) \tag{8}$$

$$\sigma_c = P - \frac{\sigma_pA_p}{A_c} \tag{9}$$

Once a local bond-slip relationship $f(\delta)$ is given, interfacial behaviour can be simulated and validated against the experimental data. Various local bond-slip laws have been developed in the last several decades, for example, the well-recognized modified Bertero-Eligehausen-Popov (mBEP) model and the Cosenza-Manfredi-Realfonzo (CMR) model [17, 29]. However, the above equilibrium equations cannot be solved in a closed form using those bond-slip models, where computing software are necessary to simulate the interfacial behaviour iteratively. In order to obtain a closed form solution, the simplified trilinear or bilinear (special case of a trilinear model) bond-slip laws are more favourable, e.g. [35]. This paper adopts a trilinear bond-slip law, which has been well recognised and used by other researchers [43, 44, 46]. Eq. (10) and Figure 2 demonstrate the trilinear model used in this paper.

The interfacial shear stress increases linearly with the interfacial slip until it reaches the peak stress τ_f at which point the value of the slip is denoted by δ_1. Interfacial softening (or micro-cracking) then starts with the shear stress reducing linearly with the increase of the interfacial slip. Shear fracture (or debonding) occurs when the interfacial slip reaches a value of δ_2. The residual shear stress τ_r implies the friction and aggregate interlock over the debonded length. $\tau_r = 0$ indicates no friction along the debonded length, which yields a bilinear local bond-slip relation, and is commonly used for externally-bonded FRP strengthened structures [26-28] as a simplification. Depending on the parent material which FRP is bonded to, the bond-slip relation may change [45].

Considering both positive and negative slip, the bond-slip model shown in Figure 2 is mathematically described in Eq. (10):

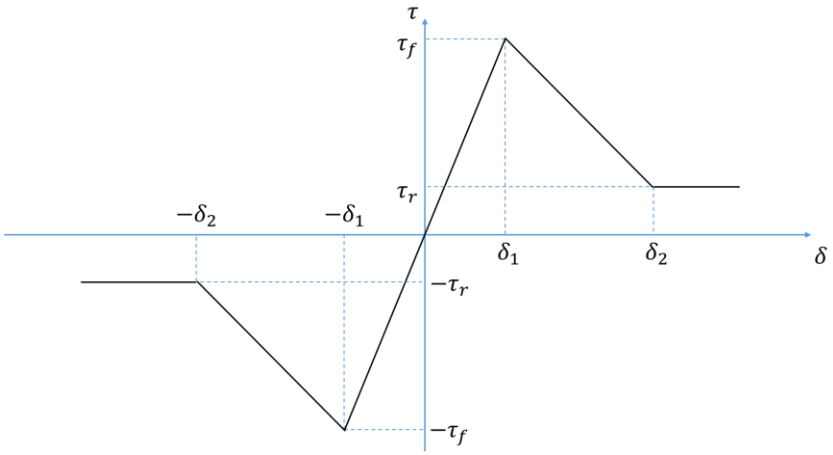

Figure 2 Local bond-slip law

$$f(\delta)=\begin{cases}-\tau_r & \delta \le -\delta_2 \\ -\frac{\tau_f-\tau_r}{\delta_2-\delta_1}\delta-\frac{\tau_f\delta_2-\tau_r\delta_1}{\delta_2-\delta_1} & -\delta_2 \le \delta \le -\delta_1 \\ \frac{\tau_f}{\delta_1}\delta & |\delta| \le \delta_1 \\ -\frac{\tau_f-\tau_r}{\delta_2-\delta_1}\delta+\frac{\tau_f\delta_2-\tau_r\delta_1}{\delta_2-\delta_1} & \delta_1 \le \delta \le \delta_2 \\ \tau_r & \delta \ge \delta_2 \end{cases} \quad (10)$$

Using the bond-slip model defined in Eq. (10), the governing equation (7) can be solved to find the shear stress distribution along the interface and the load-displacement response of a member. According to the bond-slip model defined in Eq. (10), the governing equation (7) could be written in five different forms depending on the magnitude of the slip δ:

$$\frac{d^2\delta}{dx^2}-{\lambda_1}^2\,\delta=0 \qquad -\delta_1 \le \delta \le \delta_1 \quad (11)$$

$$\frac{d^2\delta}{dx^2}+{\lambda_2}^2\,\delta={\lambda_2}^2\,e \qquad \delta_1 \le \delta \le \delta_2 \quad (12)$$

$$\frac{d^2\delta}{dx^2}+{\lambda_2}^2\,\delta=-{\lambda_2}^2\,e \qquad -\delta_2 \le \delta \le -\delta_1 \quad (13)$$

$$\frac{d^2\delta}{dx^2}-\lambda^2\,\tau_r=0 \qquad \delta \ge \delta_2 \quad (14)$$

$$\frac{d^2\delta}{dx^2}+\lambda^2\,\tau_r=0 \qquad \delta \le -\delta_2 \quad (15)$$

where

$${\lambda_1}^2=\lambda^2\frac{\tau_f}{\delta_1} \quad (16)$$

$${\lambda_2}^2=\lambda^2\frac{\tau_f-\tau_r}{\delta_2-\delta_1} \quad (17)$$

and

$$e=\frac{\tau_f\delta_2-\tau_r\delta_1}{\tau_f-\tau_r} \quad (18)$$

By solving the ordinary differential equations (ODE) in Eqs. (11) – (15), the 'generic' solutions of Eqs. (19) – (23) could be found with unknown coefficients $C_1 \sim C_{10}$, which are to be determined by using boundary conditions.

$$\delta=C_1e^{\lambda_1 x}+C_2e^{-\lambda_1 x} \qquad -\delta_1 \le \delta \le \delta_1 \quad (19)$$

$$\delta=C_3\cos(\lambda_2 x)+C_4\sin(\lambda_2 x)+e \qquad \delta_1 \le \delta \le \delta_2 \quad (20)$$

$$\delta=C_5\cos(\lambda_2 x)+C_6\sin(\lambda_2 x)-e \qquad -\delta_2 \le \delta \le -\delta_1 \quad (21)$$

$$\delta=\frac{\lambda^2\,\tau_r}{2}x^2+C_7x+C_8 \qquad \delta \ge \delta_2 \quad (22)$$

$$\delta=-\frac{\lambda^2\,\tau_r}{2}x^2+C_9x+C_{10} \qquad \delta \le -\delta_2 \quad (23)$$

At a certain load level, a given location on the interface may be in one of the three possible states: (1) elastic ($|\delta| \le \delta_1$, denoted as State I); (2) softening ($\delta_1 \le |\delta| \le \delta_2$, denoted as state II) or debonded ($|\delta| \ge \delta_2$, denoted as state III). For convenience, the interface is denoted to be in an elastic state (or E state) if the whole interface is elastic; in elastic-softening (E-S) state if the left part of the interface (towards side A in Figure 1(a)) is in the elastic state whist the right part (towards side B in Figure 1(a)) is in the softening state; in the softening-elastic-softening (S-E-S) state if softening initiates from both ends, while elastic in the intermediate range, and so on. Note that it is assumed $P_1 \ge P_2 \ge 0$, softening and debonding will always initiate from the right end.

Figure 3 shows the interfacial shear stress distribution and the propagation of debonding, when the bonded length L is sufficiently large, e.g. significantly larger than the effective bond

length. During the whole loading process, the interface may experience all or some of the stages shown in Figure 3. The solutions of all stages are presented in the following sections, and detailed debonding analysis will be demonstrated using numerical examples later in the paper.

(a) Elastic state

(b) Elastic-Softening State

(c) Softening-Elastic-Softening State – Case 1

(d) Softening-Elastic-Softening State – Case 2

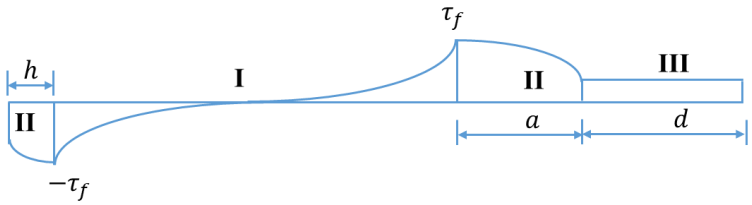

(e) Softening-Elastic-Softening-Debonding State – Case 1

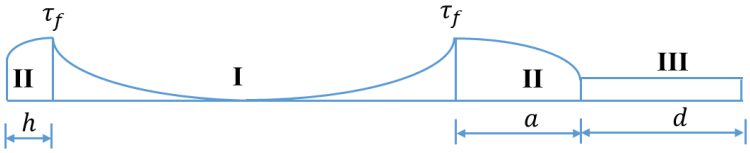

(f) Softening-Elastic-Softening-Debonding State – Case 2

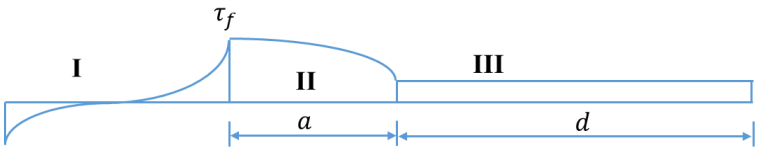

(g) Elastic-Softening-Debonding State

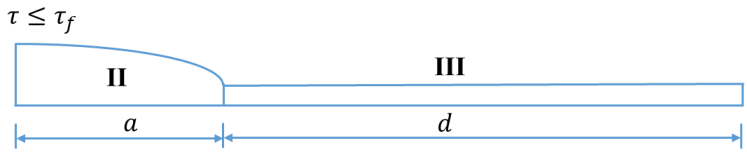

(h) Softening-Debonding State

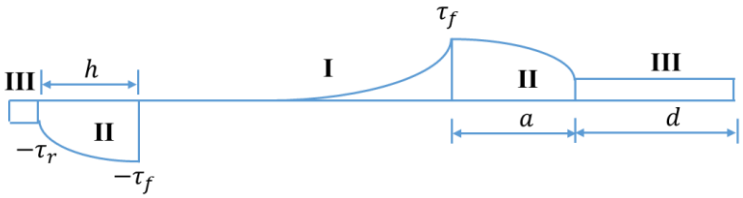

(i) Debonding-softening-elastic-softening-debonding – Case 1

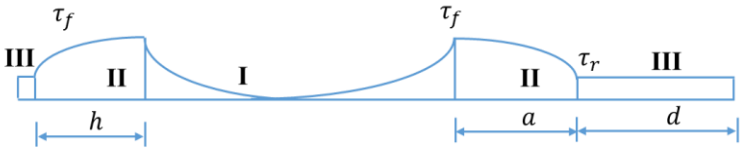

(j) Debonding-softening-elastic-softening-debonding – Case 2

Figure 3 Interfacial shear stress distribution and propagation of debonding for a large bond length

3. Analytical solutions of all stages

3.1. Elastic stage

At the beginning of loading, the entire length of the interface is in an elastic stress state (state I, Figure 3(a)), until the interfacial shear stress at x=L reaches τ_f. The governing Eq. (7) can be rewritten as Eq. (11), which has a solution described in Eq. (19). Using the boundary conditions of

$$\sigma_p = \frac{P_2}{A_p} \; at \; x = 0 \tag{24}$$

$$\text{and } \sigma_p = \frac{P_1}{A_p} \; at \; x = L \tag{25}$$

the unknown coefficients of C_1 and C_2 can be obtained. Thereby the solution of δ can be described as:

$$\delta = \left[\left(\frac{P_1}{E_pA_p} + \frac{P_3}{E_cA_c}\right)\frac{1}{\lambda_1 \sinh(\lambda_1 L)} - \left(\frac{P_2}{E_pA_p} + \frac{P_4}{E_cA_c}\right)\frac{1}{\lambda_1 \tanh(\lambda_1 L)}\right]\cosh(\lambda_1 x) + \left(\frac{P_2}{E_pA_p} + \frac{P_4}{E_cA_c}\right)\frac{1}{\lambda_1}\sinh(\lambda_1 x) \tag{26}$$

and thus the interfacial shear stress and the axial stress in the reinforcement are:

$$\tau = \frac{\tau_f}{\delta_1}\delta \tag{27}$$

$$\sigma_p = \frac{1}{A_p\gamma}\left\{\left[\left(\frac{P_1}{E_pA_p} + \frac{P_3}{E_cA_c}\right)\frac{1}{\sinh(\lambda_1 L)} - \left(\frac{P_2}{E_pA_p} + \frac{P_4}{E_cA_c}\right)\frac{1}{\tanh(\lambda_1 L)}\right]\sinh(\lambda_1 x) + \left(\frac{P_2}{E_pA_p} + \frac{P_4}{E_cA_c}\right)\cosh(\lambda_1 x) + \frac{P}{E_cA_c}\right\} \tag{28}$$

Eqs. (26-28) are identical to Teng et al. [24] by replacing the contact width b_p with the contact perimeter $\pi\phi$. The slip at the left end (Δ_0) and that at the right end (Δ_l) can be obtained by evaluating Eq. (26) at $x = 0$ and $x = L$ respectively:

$$\Delta_0 = \left[\left(\frac{P_1}{E_pA_p}+\frac{P_3}{E_cA_c}\right)\frac{1}{\lambda_1\sinh(\lambda_1 L)}-\left(\frac{P_2}{E_pA_p}+\frac{P_4}{E_cA_c}\right)\frac{1}{\lambda_1\tanh(\lambda_1 L)}\right] \quad (29)$$

$$\Delta_l = \left[\left(\frac{P_1}{E_pA_p}+\frac{P_3}{E_cA_c}\right)\frac{1}{\lambda_1\tanh(\lambda_1 L)}-\left(\frac{P_2}{E_pA_p}+\frac{P_4}{E_cA_c}\right)\frac{1}{\lambda_1\sinh(\lambda_1 L)}\right] \quad (30)$$

Defining $\beta = P_2/P_1$ and $\eta = P_3/P_1$, P_4 and P can be expressed in terms of β ($\beta \le 1$), η and P_1 from Eq. (2):

$$P_4 = (\beta+\eta-1)P_1 \quad (31)$$

$$P = (1-\eta)P_1 \quad (32)$$

Therefore Eqs. (29) and (30) could be rewritten as:

$$\Delta_0 = \left[\left(\frac{1}{E_pA_p}+\frac{\eta}{E_cA_c}\right)\frac{1}{\lambda_1\sinh(\lambda_1 L)}-\left(\frac{\beta}{E_pA_p}+\frac{\beta+\eta-1}{E_cA_c}\right)\frac{1}{\lambda_1\tanh(\lambda_1 L)}\right]P_1 \quad (33)$$

$$\Delta_l = \left[\left(\frac{1}{E_pA_p}+\frac{\eta}{E_cA_c}\right)\frac{1}{\lambda_1\tanh(\lambda_1 L)}-\left(\frac{\beta}{E_pA_p}+\frac{\beta+\eta-1}{E_cA_c}\right)\frac{1}{\lambda_1\sinh(\lambda_1 L)}\right]P_1 \quad (34)$$

It is indicated that $\Delta_l \ge |\Delta_0|$. Therefore, the softening appears either at x=L if $\beta < 1$ or simultaneously at x=0 and x=L if $\beta = 1$.

Note that the elastically bonded stage of the interface ends when Δ_l reaches δ_1. Therefore the load P_1 at the elastic limit is:

$$P_{1,elastic\ limit} = \frac{\delta_1}{\left[\left(\frac{1}{E_pA_p}+\frac{\eta}{E_cA_c}\right)\frac{1}{\lambda_1\tanh(\lambda_1 L)}-\left(\frac{\beta}{E_pA_p}+\frac{\beta+\eta-1}{E_cA_c}\right)\frac{1}{\lambda_1\sinh(\lambda_1 L)}\right]} \quad (35)$$

3.2. Elastic-softening stage

Once the load P_1 has exceeded the elastic limit, the softening commences at the right end of the interface (state II, Figure 3(b)). Part of the interface enters softening state (state II) while the rest remains elastic (state I). The load P_1 continues to increase as the length of the softening zone a increases. The ODE functions Eqs. (11) – (12) hold in this stage, which yield solutions in Eqs. (19) – (20). The boundary conditions at this stage, apart from those given by Eqs. (24) and (25), are described as below:

$$\sigma_p\ is\ continuous\ at\ x = L-a; \quad (36)$$

$$\delta = \delta_1\ or\ \tau = \tau_f\ at\ x = L-a; \quad (37)$$

Therefore the solution for the elastic region of the interface ($-\delta_1 \le \delta \le \delta_1$ or $0 \le x \le L-a$) is given by:

$$\delta = \left[\frac{\delta_1}{\cosh[\lambda_1(L-a)]}-\left(\beta\gamma+\frac{\eta-1}{E_cA_c}\right)\frac{P_1\cdot\tanh[\lambda_1(L-a)]}{\lambda_1}\right]\cosh(\lambda_1 x)+\left(\beta\gamma+\frac{\eta-1}{E_cA_c}\right)\frac{P_1}{\lambda_1}\sinh(\lambda_1 x) \quad (38)$$

$$\tau = \frac{\tau_f}{\delta_1}\delta \quad (39)$$

$$\sigma_p = \frac{\lambda_1}{A_p\gamma}\left\{\left[\frac{\delta_1}{\cosh[\lambda_1(L-a)]}-\left(\beta\gamma+\frac{\eta-1}{E_cA_c}\right)\frac{P_1\cdot\tanh[\lambda_1(L-a)]}{\lambda_1}\right]\sinh(\lambda_1 x)+\left(\beta\gamma+\frac{\eta-1}{E_cA_c}\right)\frac{P_1}{\lambda_1}\cosh(\lambda_1 x)+\frac{P}{\lambda_1 E_cA_c}\right\} \quad (40)$$

and the solution for the softening region of the interface ($\delta_1 \le \delta \le \delta_2$ or $L-a \le x \le L$) is given by:

$$\delta = (\delta_1 - e)\cos[\lambda_2(x-L+a)]+\left[\frac{\delta_1\lambda_1}{\lambda_2}\tanh[\lambda_1(L-a)]+\left(\beta\gamma+\frac{\eta-1}{E_cA_c}\right)\frac{P_1}{\lambda_2\cosh[\lambda_1(L-a)]}\right]\sin[\lambda_2(x-L+a)]+e \quad (41)$$

$$\tau = -\frac{\tau_f-\tau_r}{\delta_2-\delta_1}\delta+\frac{\tau_f\delta_2-\tau_r\delta_1}{\delta_2-\delta_1}$$

$$= \tau_f \cos[\lambda_2(x-L+a)] - \left\{\frac{\tau_f\lambda_2}{\lambda_1}\tanh[\lambda_1(L-a)] + \frac{\lambda_2}{\lambda^2}\frac{P_1\left(\beta\gamma+\frac{\eta-1}{E_cA_c}\right)}{\cosh[\lambda_1(L-a)]}\right\}\sin[\lambda_2(x-L+a)] \quad (42)$$

$$\sigma_p = \frac{1}{A_p\gamma}\left\{-\lambda_2(\delta_1-e)\sin[\lambda_2(x-L+a)] + \left[\delta_1\lambda_1\tanh[\lambda_1(L-a)] + \left(\beta\gamma+\frac{\eta-1}{E_cA_c}\right)\frac{P_1}{\cosh[\lambda_1(L-a)]}\right]\cos[\lambda_2(x-L+a)] + \frac{P}{E_cA_c}\right\} \quad (43)$$

Substituting the boundary conditions Eq. (37) into Eq. (43) yields

$$P_1 = \frac{\{(e-\delta_1)\lambda_2\sin(\lambda_2 a)+\delta_1\lambda_1\tanh[\lambda_1(L-a)]\cos(\lambda_2 a)\}\cdot\cosh[\lambda_1(L-a)]}{\left(\frac{1}{E_pA_p}+\frac{\eta}{E_cA_c}\right)\cosh[\lambda_1(L-a)]-\left(\beta\gamma+\frac{\eta-1}{E_cA_c}\right)\cos(\lambda_2 a)} \quad (44)$$

If $a = 0$, Eq. (44) returns to Eq. (35). If $\tau_r = 0$, the governing equations and solutions are identical to the equations in Teng et al. [27].

The slip at the left end (Δ_0) and that at the right end (Δ_l) can be obtained from Eqs. (38) and (41):

$$\Delta_0 = \left[\frac{\delta_1}{\cosh[\lambda_1(L-a)]} - \left(\beta\gamma+\frac{\eta-1}{E_cA_c}\right)\frac{P_1\cdot\tanh[\lambda_1(L-a)]}{\lambda_1}\right] \quad (45)$$

$$\Delta_l = (\delta_1-e)\cos(\lambda_2 a) + \left[\frac{\delta_1\lambda_1}{\lambda_2}\tanh[\lambda_1(L-a)] + \left(\beta\gamma+\frac{\eta-1}{E_cA_c}\right)\frac{P_1}{\lambda_2\cosh[\lambda_1(L-a)]}\right]\sin(\lambda_2 a) + e \quad (46)$$

3.3. Softening-elastic-softening stage

When the absolute values of both Δ_0 and Δ_l exceed δ_1, the interface enters softening-elastic-softening (S-E-S) stage. Depending on the loading conditions at the left end, the reinforcement at the left end may retract (Case 1, as shown in Figure 3 (c)) or pull out (Case 2, as shown in Figure 3(d)). Assuming the lengths of the softening zones at the left and right ends as *h* and *a* respectively, the governing equations Eqs. (11) – (13) can be solved using the following boundary conditions:

$$\sigma_p \text{ is continuous at } x = h \text{ and } x = L-a; \quad (47)$$

$$\delta = -\delta_1 \text{ or } \tau = -\tau_f \text{ at } x = h \text{ for Case 1;} \quad (48)$$

$$\text{or } \delta = \delta_1 \text{ or } \tau = \tau_f \text{ at } x = h \text{ for Case 2;} \quad (49)$$

$$\delta = \delta_1 \text{ or } \tau = \tau_f \text{ at } x = L-a; \quad (50)$$

In the Case 1, the solution for the left softening region of the interface ($-\delta_2 \le \delta \le -\delta_1$ or $0 \le x \le h$) is given by:

$$\delta = (e-\delta_1)\cos[\lambda_2(x-h)] + \delta_1\frac{\lambda_1}{\lambda_2}\coth[0.5\lambda_1(L-a-h)]\sin[\lambda_2(x-h)] - e \quad (51)$$

$$\tau = -\frac{\tau_f-\tau_r}{\delta_2-\delta_1}\delta - \frac{\tau_f\delta_2-\tau_r\delta_1}{\delta_2-\delta_1} = -\tau_f\cos[\lambda_2(x-h)] - \left\{\frac{\tau_f-\tau_r}{\delta_2-\delta_1}\delta_1\frac{\lambda_1}{\lambda_2}\coth[0.5\lambda_1(L-a-h)]\right\}\sin[\lambda_2(x-h)] \quad (52)$$

$$\sigma_p = \frac{1}{A_p\gamma}\left\{-(e-\delta_1)\lambda_2\sin[\lambda_2(x-h)] + \delta_1\lambda_1\coth[0.5\lambda_1(L-a-h)]\cos[\lambda_2(x-h)] + \frac{P}{E_cA_c}\right\} \quad (53)$$

The solution for the elastic region of the interface ($-\delta_1 \le \delta \le \delta_1$ or $h \le x \le L-a$) is given by:

$$\delta = -\delta_1 \cosh[\lambda_1(x-h)] + \delta_1 \coth[0.5\lambda_1(L-a-h)] \sinh[\lambda_1(x-h)] \quad (54)$$

$$\tau = -\tau_f \cosh[\lambda_1(x-h)] + \tau_f \coth[0.5\lambda_1(L-a-h)] \sinh[\lambda_1(x-h)] \quad (55)$$

$$\sigma_p = \frac{1}{A_p\gamma}\left\{-\delta_1\lambda_1 \sinh[\lambda_1(x-h)] + \delta_1\lambda_1 \coth[0.5\lambda_1(L-a-h)] \cosh[\lambda_1(x-h)] + \frac{P}{E_cA_c}\right\} \quad (56)$$

The solution for the right softening region of the interface ($\delta_1 \le \delta \le \delta_2$ or $L-a \le x \le L$) is given by:

$$\delta = -(e-\delta_1)\cos[\lambda_2(x-L+a)] + \delta_1\frac{\lambda_1}{\lambda_2}\coth[0.5\lambda_1(L-a-h)]\sin[\lambda_2(x-L+a)] + e \quad (57)$$

$$\tau = -\frac{\tau_f-\tau_r}{\delta_2-\delta_1}\delta + \frac{\tau_f\delta_2-\tau_r\delta_1}{\delta_2-\delta_1} = \tau_f\cos[\lambda_2(x-L+a)] - \left\{\frac{\tau_f-\tau_r}{\delta_2-\delta_1}\delta_1\frac{\lambda_1}{\lambda_2}\coth[0.5\lambda_1(L-a-h)]\right\}\sin[\lambda_2(x-L+a)] \quad (58)$$

$$\sigma_p = \frac{1}{A_p\gamma}\left\{(e-\delta_1)\lambda_2\sin[\lambda_2(x-L+a)] + \delta_1\lambda_1\coth[0.5\lambda_1(L-a-h)]\cos[\lambda_2(x-L+a)] + \frac{P}{E_cA_c}\right\} \quad (59)$$

Using the boundary conditions stated in Eqs. (24) and (25), the relation between *h* and *a* can be obtained through the two simultaneous equations (60) and (61).

$$P_1 = \frac{1}{\frac{\beta}{E_pA_p}+\frac{\beta+\eta-1}{E_cA_c}}\{\delta_1\lambda_1\coth[0.5\lambda_1(L-a-h)]\cos(\lambda_2h) + (e-\delta_1)\lambda_2\sin(\lambda_2h)\} \quad (60)$$

$$P_1 = \frac{1}{\frac{1}{E_pA_p}+\frac{\eta}{E_cA_c}}\{\delta_1\lambda_1\coth[0.5\lambda_1(L-a-h)]\cos(\lambda_2a) + (e-\delta_1)\lambda_2\sin(\lambda_2a)\} \quad (61)$$

The slip at the left end (Δ_0) and that at the right end (Δ_l) can be obtained from Eqs. (62) and (63):

$$\Delta_0 = (e-\delta_1)\cos(\lambda_2h) - \delta_1\frac{\lambda_1}{\lambda_2}\coth[0.5\lambda_1(L-a-h)]\sin(\lambda_2h) - e \quad (62)$$

$$\Delta_l = -(e-\delta_1)\cos(\lambda_2a) + \delta_1\frac{\lambda_1}{\lambda_2}\coth[0.5\lambda_1(L-a-h)]\sin(\lambda_2a) + e \quad (63)$$

In the Case 2, the solutions are obtained as:

The left softening region of the interface ($\delta_1 \le \delta \le \delta_2$ or $0 \le x \le h$):

$$\delta = (\delta_1-e)\cos[\lambda_2(x-h)] - \delta_1\frac{\lambda_1}{\lambda_2}\tanh[0.5\lambda_1(L-a-h)]\sin[\lambda_2(x-h)] + e \quad (64)$$

$$\tau = -\frac{\tau_f-\tau_r}{\delta_2-\delta_1}\delta + \frac{\tau_f\delta_2-\tau_r\delta_1}{\delta_2-\delta_1} = \tau_f\cos[\lambda_2(x-h)] + \left\{\frac{\tau_f-\tau_r}{\delta_2-\delta_1}\delta_1\frac{\lambda_1}{\lambda_2}\tanh[0.5\lambda_1(L-a-h)]\right\}\sin[\lambda_2(x-h)] \quad (65)$$

$$\sigma_p = \frac{1}{A_p\gamma}\left\{-(\delta_1-e)\lambda_2\sin[\lambda_2(x-h)] - \delta_1\lambda_1\tanh[0.5\lambda_1(L-a-h)]\cos[\lambda_2(x-h)] + \frac{P}{E_cA_c}\right\} \quad (66)$$

The elastic region of the interface ($0 \le \delta \le \delta_1$ or $h \le x \le L-a$):

$$\delta = \delta_1\cosh[\lambda_1(x-h)] - \delta_1\tanh[0.5\lambda_1(L-a-h)]\sinh[\lambda_1(x-h)] \quad (67)$$

$$\tau = \tau_f \cosh[\lambda_1(x-h)] - \tau_f \tanh[0.5\lambda_1(L-a-h)] \sinh[\lambda_1(x-h)] \quad (68)$$

$$\sigma_p = \frac{1}{A_p\gamma}\left\{\delta_1\lambda_1 \sinh[\lambda_1(x-h)] - \delta_1\lambda_1 \tanh[0.5\lambda_1(L-a-h)] \cosh[\lambda_1(x-h)] + \frac{P}{E_cA_c}\right\} \quad (69)$$

The right softening region of the interface ($\delta_1 \le \delta \le \delta_2$ or $L-a \le x \le L$):

$$\delta = (\delta_1 - e)\cos[\lambda_2(x-L+a)] + \delta_1\frac{\lambda_1}{\lambda_2}\tanh[0.5\lambda_1(L-a-h)]\sin[\lambda_2(x-L+a)] + e \quad (70)$$

$$\tau = -\frac{\tau_f-\tau_r}{\delta_2-\delta_1}\delta + \frac{\tau_f\delta_2-\tau_r\delta_1}{\delta_2-\delta_1}$$
$$= \tau_f \cos[\lambda_2(x-L+a)] - \left\{\frac{\tau_f-\tau_r}{\delta_2-\delta_1}\delta_1\frac{\lambda_1}{\lambda_2}\tanh[0.5\lambda_1(L-a-h)]\right\}\sin[\lambda_2(x-L+a)] \quad (71)$$

$$\sigma_p = \frac{1}{A_p\gamma}\left\{(e-\delta_1)\lambda_2 \sin[\lambda_2(x-L+a)] + \delta_1\lambda_1 \tanh[0.5\lambda_1(L-a-h)]\cos[\lambda_2(x-L+a)] + \frac{P}{E_cA_c}\right\} \quad (72)$$

The relation between h and a:

$$P_1 = \frac{1}{\frac{\beta}{E_pA_p}+\frac{\beta+\eta-1}{E_cA_c}}\{-\delta_1\lambda_1 \tanh[0.5\lambda_1(L-a-h)]\cos(\lambda_2 h) - (e-\delta_1)\lambda_2 \sin(\lambda_2 h)\} \quad (73)$$

$$P_1 = \frac{1}{\frac{1}{E_pA_p}+\frac{\eta}{E_cA_c}}\{\delta_1\lambda_1 \tanh[0.5\lambda_1(L-a-h)]\cos(\lambda_2 a) + (e-\delta_1)\lambda_2 \sin(\lambda_2 a)\} \quad (74)$$

The slip at the left end (Δ_0) and that at the right end (Δ_l) can be obtained from Eqs. (75) and (76):

$$\Delta_0 = -(e-\delta_1)\cos(\lambda_2 h) + \delta_1\frac{\lambda_1}{\lambda_2}\tanh[0.5\lambda_1(L-a-h)]\sin(\lambda_2 h) + e \quad (75)$$

$$\Delta_l = (e-\delta_1)\cos(\lambda_2 a) + \delta_1\frac{\lambda_1}{\lambda_2}\tanh[0.5\lambda_1(L-a-h)]\sin(\lambda_2 a) + e \quad (76)$$

If $\beta = 1$, Eqs. (60-63) yield that $a = h$ and $\Delta_0 = \Delta_l$.

3.4. Elastic-softening-debonding stage

During this stage, the debonding commences at the right end and propagates along the interface (Figure 3(g)). It usually occurs when β is very small and the bonded length is relatively large. Assuming that the debonded length is d and the softening distance is a, the governing equations (11), (12) and (14) can be solved using the boundary conditions in Eqs. (77) – (79):

$$\sigma_p \text{ is continuous at } x = L-d-a \text{ and } x = L-d; \quad (77)$$

$$\delta = \delta_1 \text{ or } \tau = \tau_f \text{ at } x = L-d-a\,; \quad (78)$$

$$\delta = \delta_2 \text{ or } \tau = \tau_r \text{ at } x = L-d; \quad (79)$$

The solutions of the elastic region of the interface ($-\delta_1 \le \delta \le \delta_1$ or $0 \le x \le L-d-a$):

$$\delta = \delta_1 \cosh[\lambda_1(x-L+a+d)] + \frac{\lambda_2}{\lambda_1}\frac{(\delta_2-e)+(e-\delta_1)\cos(\lambda_2 a)}{\sin(\lambda_2 a)}\sinh[\lambda_1(x-L+a+d)] \quad (80)$$

$$\tau = \frac{\tau_f}{2}\cosh[\lambda_1(x-L+a+d)] + \frac{\tau_f}{\delta_1}\frac{\lambda_2}{\lambda_1}\frac{(\delta_2-e)+(e-\delta_1)\cos(\lambda_2 a)}{2\sin(\lambda_2 a)}\sinh[\lambda_1(x-L+a+d)] \quad (81)$$

$$\sigma_p = \frac{1}{A_p\gamma}\left\{\delta_1\lambda_1 \sinh[\lambda_1(x-L+a+d)] + \lambda_2 \frac{(\delta_2-e)+(e-\delta_1)\cos(\lambda_2 a)}{\sin(\lambda_2 a)} \cosh[\lambda_1(x-L+a+d)] + \frac{P}{E_c A_c}\right\} \quad (82)$$

The solution for the softening region of the interface ($\delta_1 \le \delta \le \delta_2$ or $L-d-a \le x \le L-d$) is given by:

$$\delta = -\frac{\delta_1-e}{\sin(\lambda_2 a)}\sin[\lambda_2(x-L+d)] + \frac{\delta_2-e}{\sin(\lambda_2 a)}\sin[\lambda_2(x-L+d+a)] + e \quad (83)$$

$$\tau = -\frac{\tau_f-\tau_r}{\delta_2-\delta_1}\delta + \frac{\tau_f\delta_2-\tau_r\delta_1}{\delta_2-\delta_1} = -\tau_f\frac{\sin[\lambda_2(x-L+d)]}{\sin(\lambda_2 a)} + \tau_r\frac{\sin[\lambda_2(x-L+d+a)]}{\sin(\lambda_2 a)} \quad (84)$$

$$\sigma_p = \frac{1}{A_p\gamma}\left\{-\lambda_2(\delta_1-e)\frac{\cos[\lambda_2(x-L+d)]}{\sin(\lambda_2 a)} + \lambda_2(\delta_2-e)\frac{\cos[\lambda_2(x-L+d+a)]}{\sin(\lambda_2 a)} + \frac{P}{E_c A_c}\right\} \quad (85)$$

The solution for the debonded region of the interface ($\delta \ge \delta_2$ or $L-d \le x \le L$) is given by:

$$\delta = \frac{\lambda^2\tau_r}{2}(x-L+d)^2 + \lambda_2\frac{(e-\delta_1)+(\delta_2-e)\cos(\lambda_2 a)}{\sin(\lambda_2 a)}(x-L+d) + \delta_2 \quad (86)$$

$$\tau = \tau_r \quad (87)$$

$$\sigma_p = \frac{1}{A_p\gamma}\left\{\lambda^2\tau_r(x-L+d) + \lambda_2\frac{(e-\delta_1)+(\delta_2-e)\cos(\lambda_2 a)}{\sin(\lambda_2 a)} + \frac{P}{E_c A_c}\right\} \quad (88)$$

The slip at the left end (Δ_0) and that at the right end (Δ_l) can be obtained from Eqs. (80) and (86):

$$\Delta_0 = \frac{\delta_1}{2}\cosh[\lambda_1(L-a-d)] - \frac{\lambda_2}{\lambda_1}\frac{(\delta_2-e)+(e-\delta_1)\cos(\lambda_2 a)}{2\sin(\lambda_2 a)}\sinh[\lambda_1(L-a-d)] \quad (89)$$

$$\Delta_l = \frac{\lambda^2\tau_r}{2}d^2 + \lambda_2\frac{(e-\delta_1)+(\delta_2-e)\cos(\lambda_2 a)}{\sin(\lambda_2 a)}d + \delta_2 \quad (90)$$

3.5. Softening-elastic-softening-debonding stage

When debonding initiates at the right end (side B in Figure 1(b)) of the S-E-S interface, the interface enters the S-E-S-D stage. Depending on the direction of the relative slip at the left end, the interfacial stress in the S-E-S-D stage could be presented as Case 1 (Figure 3(e)) or Case 2 (Figure 3(f)). As the debonding propagates, the peak shear stress τ_f near the right end moves towards the left. Under the assumption that the whole local bond-slip model is fully reversible before debonding, the peak shear stress τ_f near the left end also moves towards the left. Therefore, the left softening zone will experience unloading although the actual applied load increases. Assuming the debonded length of the interface at the right as *d*, Eqs. (51) – (59) and Eqs. (64) – (72) remain valid if the bonded length *L* is replaced by (*L*-*d*). The solutions of the debonded range can be obtained by using the boundary conditions

$$\sigma_p \text{ is continuous at } x = L-d; \quad (91)$$

$$\delta = \delta_2 \text{ or } \tau = \tau_r \text{ at } x = L-d; \quad (92)$$

In the Case 1, the solutions of the softening and elastic ranges can be obtained by replacing *L* in Eqs. (51) – (59) with (*L*-*d*). The solution for the debonded range can be obtained by solving the governing equation (14) using Eqs. (91) – (92):

$$\delta = \frac{\lambda^2\tau_r}{2}(x-L+d)^2 + \{\delta_1\lambda_1\coth[0.5\lambda_1(L-a-d-h)]\cos(\lambda_2 a) - (\delta_1-e)\lambda_2\sin(\lambda_2 a)\}(x-L+d) + \delta_2 \quad (93)$$

$$\tau = \tau_f \quad (94)$$

$$\sigma_p = \frac{1}{A_p\gamma}\left\{\lambda^2\,\tau_r(x-L+d) + \delta_1\lambda_1\coth[0.5\lambda_1(L-a-d-h)]\cos(\lambda_2 a) - (\delta_1 - e)\lambda_2\sin(\lambda_2 a) + \frac{P}{E_cA_c}\right\} \quad (95)$$

The slip at the left end (Δ_0) and that at the right end (Δ_l) can be found as:

$$\Delta_0 = (e-\delta_1)\cos(\lambda_2 h) - \delta_1\frac{\lambda_1}{\lambda_2}\coth[0.5\lambda_1(L-d-a-h)]\sin(\lambda_2 h) - e \quad (96)$$

$$\Delta_l = \frac{\lambda^2\,\tau_r d(d-L)}{2} + \{\delta_1\lambda_1\coth[0.5\lambda_1(L-a-d-h)]\cos(\lambda_2 a) - (\delta_1 - e)\lambda_2\sin(\lambda_2 a)\}d + \delta_2 \quad (97)$$

The relation between *a*, *h* and P_1 can be obtained using the simultaneous equations (98) – (100) obtained using boundary conditions in Eqs. (24) and (25), and the continuous boundary at *x*=*L*-*d* (Eqs. (91) and (92)):

$$\coth[0.5\lambda_1(L-a-d-h)] = \frac{\lambda_2[(\delta_2-e)-(\delta_1-e)\cos(\lambda_2 a)]}{\delta_1\lambda_1\sin(\lambda_2 a)} \quad (98)$$

$$P_1 = \frac{1}{\frac{\beta}{E_pA_p}+\frac{\beta+\eta-1}{E_cA_c}}\{-(\delta_1-e)\lambda_2\sin(\lambda_2 h) + \delta_1\lambda_1\coth[0.5\lambda_1(L-d-a-h)]\cos(\lambda_2 h)\} \quad (99)$$

$$P_1 = \frac{1}{\frac{1}{E_pA_p}+\frac{\eta}{E_cA_c}}\{\lambda^2\,\tau_r d - (\delta_1-e)\lambda_2\sin(\lambda_2 a) + \delta_1\lambda_1\coth[0.5\lambda_1(L-a-d-h)]\cos(\lambda_2 a)\} \quad (100)$$

In the Case 2, the solutions of the softening and elastic ranges can be obtained by replacing *L* in Eqs. (64) – (72) with (*L*-*d*). The solution for the debonded range is:

$$\delta = \frac{\lambda^2\,\tau_r}{2}(x-L+d)^2 + \{\delta_1\lambda_1\tanh[0.5\lambda_1(L-a-d-h)]\cos(\lambda_2 a) - (\delta_1 - e)\lambda_2\sin(\lambda_2 a)\}(x-L+d) + \delta_2 \quad (101)$$

$$\tau = \tau_f \quad (102)$$

$$\sigma_p = \frac{1}{A_p\gamma}\left\{\lambda^2\,\tau_r(x-L+d) + \delta_1\lambda_1\tanh[0.5\lambda_1(L-a-d-h)]\cos(\lambda_2 a) - (\delta_1 - e)\lambda_2\sin(\lambda_2 a) + \frac{P}{E_cA_c}\right\} \quad (103)$$

The slip at the left end (Δ_0) and that at the right end (Δ_l) are then:

$$\Delta_0 = (\delta_1-e)\cos(\lambda_2 h) + \delta_1\frac{\lambda_1}{\lambda_2}\tanh[0.5\lambda_1(L-d-a-h)]\sin(\lambda_2 h) + e \quad (104)$$

$$\Delta_l = \frac{\lambda^2\,\tau_r}{2}d^2 + \{\delta_1\lambda_1\tanh[0.5\lambda_1(L-a-d-h)]\cos(\lambda_2 a) - (\delta_1-e)\lambda_2\sin(\lambda_2 a)\}d + \delta_2 \quad (105)$$

The relation between *a*, *h* and P_1 can be found using the simultaneous equations (106) – (108) obtained using boundary conditions at the two ends (Eqs. (24) and (25), and the continuous boundary at *x*=*L*-*d* (Eqs. (91) and (92)):

$$\tanh[0.5\lambda_1(L-a-d-h)] = \frac{\lambda_2[(\delta_2-e)-(\delta_1-e)\cos(\lambda_2 a)]}{\delta_1\lambda_1\sin(\lambda_2 a)} \quad (106)$$

$$P_1 = \frac{1}{\frac{\beta}{E_pA_p}+\frac{\beta+\eta-1}{E_cA_c}}\{(\delta_1-e)\lambda_2\sin(\lambda_2 h) - \delta_1\lambda_1\tanh[0.5\lambda_1(L-d-a-h)]\cos(\lambda_2 h)\} \quad (107)$$

$$P_1 = \frac{1}{\frac{1}{E_pA_p}+\frac{\eta}{E_cA_c}}\{\lambda^2\,\tau_r d - (\delta_1 - e)\lambda_2 \sin(\lambda_2 a) + \delta_1\lambda_1 \tanh[0.5\lambda_1(L-a-d-h)]\cos(\lambda_2 a)\} \quad (108)$$

3.6. Softening stage

If the bonding length is so short that the interface does not experience a debonding stage during the failure process, the whole interface is governed by Eq. (12) with the load boundary conditions at the two ends. The following solutions are then found:

$$\delta = \frac{1}{\lambda_2}\left[\left(\frac{\beta}{E_pA_p}+\frac{\beta+\eta-1}{E_cA_c}\right)\frac{1}{\tan(\lambda_2 L)} - \left(\frac{1}{E_pA_p}+\frac{\eta}{E_cA_c}\right)\frac{1}{\sin(\lambda_2 L)}\right]P_1\cos(\lambda_2 x) + \frac{1}{\lambda_2}\left(\frac{\beta}{E_pA_p}+\frac{\beta+\eta-1}{E_cA_c}\right)P_1\sin(\lambda_2 x) + e \quad (109)$$

$$\tau = -\frac{\tau_f-\tau_r}{\delta_2-\delta_1}\delta + \frac{\tau_f\delta_2-\tau_r\delta_1}{\delta_2-\delta_1} \quad (110)$$

$$\sigma_p = \frac{1}{A_p\gamma}\left\{-\left[\left(\frac{\beta}{E_pA_p}+\frac{\beta+\eta-1}{E_cA_c}\right)\frac{1}{\tan(\lambda_2 L)} - \left(\frac{1}{E_pA_p}+\frac{\eta}{E_cA_c}\right)\frac{1}{\sin(\lambda_2 L)}\right]P_1\sin(\lambda_2 x) + \left(\frac{\beta}{E_pA_p}+\frac{\beta+\eta-1}{E_cA_c}\right)P_1\cos(\lambda_2 x) + \frac{P}{E_cA_c}\right\} \quad (111)$$

The slip at the left end (Δ_0) and that at the right end (Δ_l) can be obtained as:

$$\Delta_0 = \frac{P_1}{\lambda_2}\left[\left(\frac{\beta}{E_pA_p}+\frac{\beta+\eta-1}{E_cA_c}\right)\frac{1}{\tan(\lambda_2 L)} - \left(\frac{1}{E_pA_p}+\frac{\eta}{E_cA_c}\right)\frac{1}{\sin(\lambda_2 L)}\right] + e \quad (112)$$

$$\Delta_l = \frac{P_1}{\lambda_2}\left[\left(\frac{\beta}{E_pA_p}+\frac{\beta+\eta-1}{E_cA_c}\right)\frac{1}{\sin(\lambda_2 L)} - \left(\frac{1}{E_pA_p}+\frac{\eta}{E_cA_c}\right)\frac{1}{\tan(\lambda_2 L)}\right] + e \quad (113)$$

If $\Delta_0 = \delta_1$ and $\Delta_l = \delta_2$ occur simultaneously, the critical bond length L_{cr} can be obtained from Eq. (112) and (113):

$$L_{cr} = \frac{1}{\lambda_2}arccos\left\{\frac{(\delta_1-e)\left(\frac{\beta}{E_pA_p}+\frac{\beta+\eta-1}{E_cA_c}\right)+(\delta_2-e)\left(\frac{1}{E_pA_p}+\frac{\eta}{E_cA_c}\right)}{(\delta_2-e)\left(\frac{\beta}{E_pA_p}+\frac{\beta+\eta-1}{E_cA_c}\right)+(\delta_1-e)\left(\frac{1}{E_pA_p}+\frac{\eta}{E_cA_c}\right)}\right\} \quad (114)$$

3.7. Softening-debonding stage

The softening-debonding stage (as shown in Figure 3(h)) is governed by Eqs. (12) and (14) with the following boundary conditions:

$$\sigma_p = \frac{P_2}{A_p}\ at\ x = 0; \quad (115)$$

$$\sigma_p\ is\ continuous\ at\ x = L-d; \quad (116)$$

$$\delta = \delta_2\ or\ \tau = \tau_r\ at\ x = L-d; \quad (117)$$

$$\sigma_p = \frac{P_1}{A_p}\ at\ x = L \quad (118)$$

The solution of the softening region ($\delta_1 \le \delta \le \delta_2$ or $L-d-a \le x \le L-d$) is given by:

$$\delta = \left\{\frac{P_1}{\lambda_2}\left[\left(\frac{\beta}{E_pA_p}+\frac{\beta+\eta-1}{E_cA_c}\right)\frac{1}{\tan[\lambda_2(L-d)]} - \left(\frac{1}{E_pA_p}+\frac{\eta}{E_cA_c}\right)\frac{1}{\sin[\lambda_2(L-d)]}\right] + \frac{\pi\emptyset\tau_r d\gamma}{\lambda_2\sin[\lambda_2(L-d)]}\right\}\cos(\lambda_2 x) + \frac{P_1}{\lambda_2}\left(\frac{\beta}{E_pA_p}+\frac{\beta+\eta-1}{E_cA_c}\right)\sin(\lambda_2 x) + e \quad (119)$$

$$\tau = -\frac{\tau_f-\tau_r}{\delta_2-\delta_1}\delta + \frac{\tau_f\delta_2-\tau_r\delta_1}{\delta_2-\delta_1} \quad (120)$$

$$\sigma_p = \frac{1}{A_p\gamma}\left\{-\left\{P_1\left[\left(\frac{\beta}{E_pA_p}+\frac{\beta+\eta-1}{E_cA_c}\right)\frac{1}{\tan[\lambda_2(L-d)]} - \left(\frac{1}{E_pA_p}+\frac{\eta}{E_cA_c}\right)\frac{1}{\sin[\lambda_2(L-d)]}\right] + \frac{\pi\emptyset\tau_r d\gamma}{\sin[\lambda_2(L-d)]}\right\}\sin(\lambda_2 x) + P_1\left(\frac{\beta}{E_pA_p}+\frac{\beta+\eta-1}{E_cA_c}\right)\cos(\lambda_2 x) + \frac{P}{E_cA_c}\right\} \quad (121)$$

The solution of the debonded region ($\delta \geq \delta_2$ or $L - d \leq x \leq L$) is given by:

$$\delta = \frac{\lambda^2 \tau_r}{2}(x - L + d)^2 + \left\{\left(\frac{1}{E_p A_p} + \frac{\eta}{E_c A_c}\right) P_1 - \pi \emptyset \tau_r d\gamma \right\}(x - L + d) + \delta_2 \quad (122)$$

$$\tau = \tau_f \quad (123)$$

$$\sigma_p = \frac{1}{A_p \gamma}\left\{\lambda^2 \tau_r (x - L + d) + \left[\left(\frac{1}{E_p A_p} + \frac{\eta}{E_c A_c}\right) P_1 - \pi \emptyset \tau_r d\gamma\right] + \frac{P}{E_c A_c}\right\} \quad (124)$$

The slip at the left end (Δ_0) and that at the right end (Δ_l) can be obtained as:

$$\Delta_0 = \left\{\frac{P_1}{\lambda_2}\left[\left(\frac{\beta}{E_p A_p} + \frac{\beta+\eta-1}{E_c A_c}\right)\frac{1}{\tan[\lambda_2(L-d)]} - \left(\frac{1}{E_p A_p} + \frac{\eta}{E_c A_c}\right)\frac{1}{\sin[\lambda_2(L-d)]}\right] + \frac{\pi \emptyset \tau_r d\gamma}{\lambda_2 \sin[\lambda_2(L-d)]}\right\} + e \quad (125)$$

$$\Delta_l = -\frac{\lambda^2 \tau_r}{2} d^2 + \left(\frac{1}{E_p A_p} + \frac{\eta}{E_c A_c}\right) P_1 d + \delta_2 \quad (126)$$

3.8. Debonding-softening-elastic-softening-debonding stage

When β is smaller than 1, this stage occurs if the bond length is very large (see Figure 3 (i) and (j)). Although it is possible in theory, the concrete matrix would have failed far before this stage occurs, i.e. new cracks would have been developed, and the bond length has been significantly shortened. Unfortunately this theoretical model could not predict the location of the new emerging crack, due to the assumption of a simplified one-dimensional modelling. To enable the prediction of crack generation and crack propagation, 3D modelling is usually necessary.

When $\beta = 1$, debonding can initiate from both ends simultaneously, at the condition of $\Delta_0 = \Delta_l = \delta_2$. As stated in [27], the ultimate debonding load becomes infinite when $\beta = 1$, indicating that debonding failure does not occur under this condition. It has been explained in reference [27] that $\beta = 1$ occurs in a pure bending zone, where the crack-induced debonding does not initiate. Therefore, no analytical solutions for this situation have been given in this paper.

4. Numerical examples

The theoretical solutions derived in this paper can be easily evaluated using mathematical software such as Matlab [30]. The 'displacement control' method is applied in this research, where the relative slip at the right end (Δ_l) increases incrementally, and the corresponding load P_1 as well as the interfacial properties such as stresses and slip are evaluated for each increment. All interfacial stages have been coded in individual sub-functions. In addition, a 'switch' sub-function has been created to determine which stage the interface is to experience, based on the relative slip Δ_0 and Δ_l at the two ends, and to direct the calculation to the corresponding sub-function. It is worth noting that, limited by the nature of 'displacement control' method, the well-known snap-back phenomenon [47, 48] could not be captured in this numerical study. As the snap-back phenomenon only occurs with a sufficiently long debonded length, which is rather unlikely to occur for fibre reinforced cementitious composites, ignoring the snap-back phenomenon is considered adequate for the following case studies.

In this section, numerical examples are presented to illustrate the various interfacial failure processes and the corresponding load-slip relationship. Unless specified, the diameter of the fibre is 1.1mm, which represents the tow size of 24k carbon fibre filaments. Young's modulus of the fibre is assumed to be 230 GPa and C100 concrete is modelled as the matrix, with a Young's modulus of 45 GPa. Textile mesh sizes between 5 mm and 25 mm are commonly used in practice, which represents a concrete width of 5 mm to 25 mm for each tow. The thickness between textile layers is taken to be no larger than the mesh size. The local bond-slip law is

estimated using reference [4], where $\delta_1 = 0.01mm, \delta_2 = 0.7mm, \tau_f = 7.2MPa, and\ \tau_r = 2MPa$. The mechanical behaviour of the fibre-concrete interface will be discussed below.

4.1. Validation

Before conducting a parametric analysis, the proposed theoretical solutions are first validated using the analytical methods in references [27] and [28], as well as the FEA carried out using ANSYS [31]. Figure 4 shows the comparison between results given by the proposed analytical model in this paper and the reference [27, 28]. The same local bond-slip law and material properties are adopted as described in paper [27, 28] respectively. Figure 4(a) represents a FRP laminate strengthened concrete model between two cracks where both concrete and the FRP laminate are loaded at the two ends ($\beta = 0.8, \eta = 1$), while Figure 4(b) represents a specific case for pull-pull bonded FRP strengthened joints ($\beta = 0, \eta = 0$). Both case studies have shown very close agreement, indicating the validity of the theoretical solutions proposed in the present paper.

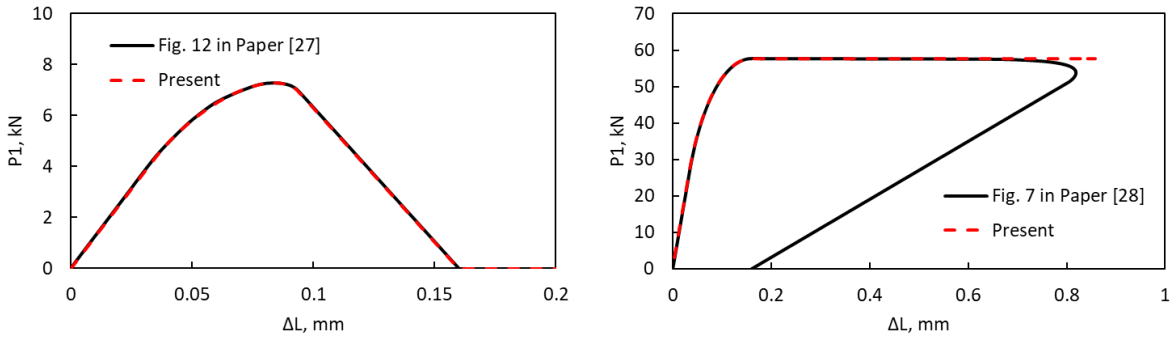

(a) $L = 10mm$ (b) L=1200mm, $\frac{E_c A_c}{E_p A_p} = 1.25$

Figure 4 Comparison of full-range load-displacement curves

A 2D asymmetric model and a 3D solid model have been created using the cohesive zone method (CZM) in the finite element method software ANSYS [31]. Elastic material properties are adopted for both the fibre and the concrete matrix. The fibre is taken as circular, with a cross-section of 1 mm^2 and the Young's modulus of 230GPa. The cross-section of the concrete is 10mm x 5mm, giving a reinforcement ratio of 2%. The Young's modulus of the concrete is taken as 45GPa, and the bond length is 30mm. Maximum mesh size of 0.5mm is adopted for the concrete, and 0.1mm for the interface (Figure 5). The local bond-slip law is estimated using reference [4], where $\delta_1 = 0.01mm, \delta_2 = 0.7mm, \tau_f = 7.2MPa, and\ \tau_r = 2MPa$.

Displacement control is used in the model, and the boundary condition is applied as $\beta = 0, and\ \eta = 0$ (pull-pull load condition). Figure 6 shows the load-displacement relation of the model using both the FEA and the theoretical model proposed in this paper. In general, the FEA solution agrees well with the theoretical solution. 3D FEA slightly overestimates the stiffness and the ultimate load of the interface, because a higher arbitrary damping was adopted in order to solve the highly nonlinear problem within reasonable running time. Since the difference between the FEA solutions and the theoretical solution are small, the theoretical method is deemed to provide valid solutions.

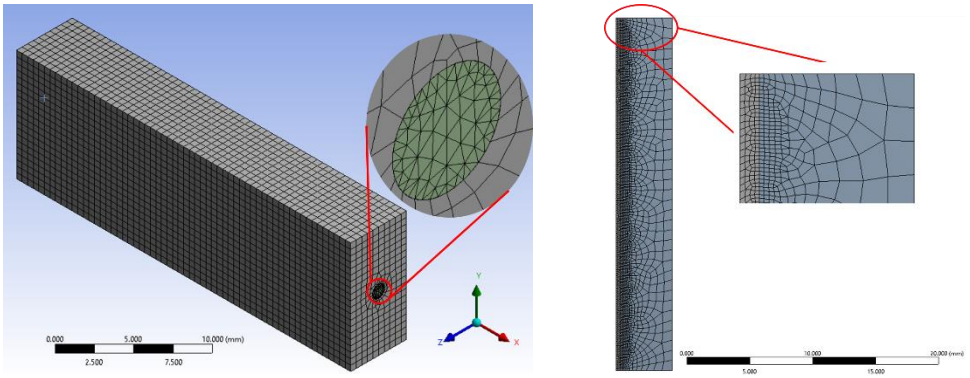

(a) 3D solid model (b) 2D asymmetric surface model

Figure 5 Mesh of both 3D and 2D models

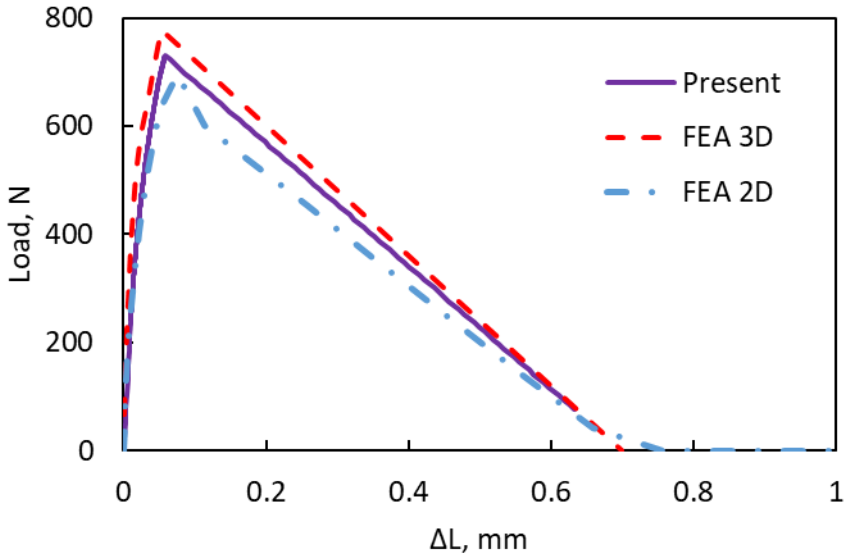

Figure 6 Comparison between FEA and the proposed theoretical model

4.2. Effect of simplified evaluation of the local bond-slip law

Pull-out tests are usually carried out to investigate local interfacial properties. However, to obtain the localised bond-slip relation is not simple. A simplified shear strength approach [13, 33] has been historically used, by assuming that the interfacial shear stress is uniformly distributed along the bond interface:

$$\tau = \frac{P}{\pi d L} \tag{127}$$

Although it is widely accepted, and has even been shown to be valid for conventional carbon steel reinforced concrete [34], the applicability of the simplified method to carbon fibre reinforced concrete is yet to be investigated. Figure 7 shows load-displacement curves for carbon fibre reinforced concrete with different bond lengths. The carbon fibre tow size for 24k filaments (diameter of 1.1mm), and a concrete cross-sectional area of 100 mm^2 are adopted, indicating a reinforcement ratio of 1%. It is shown that the simplified method could predict the bond strength reasonably well under a low aspect ratio (short bond length), but the error becomes excessive with the increase of the bond length. For example, the difference of the predicted bond strength between the simplified method and the proposed analytical method is only 1.7% when the bond length is 30 mm. However the difference reaches 21% when the bond length increases to 100 mm. In addition, the simplified method significantly overestimates the

stiffness of the interface. Therefore, the results may be misleading if one uses the simplified method to evaluate the local bond-slip relation.

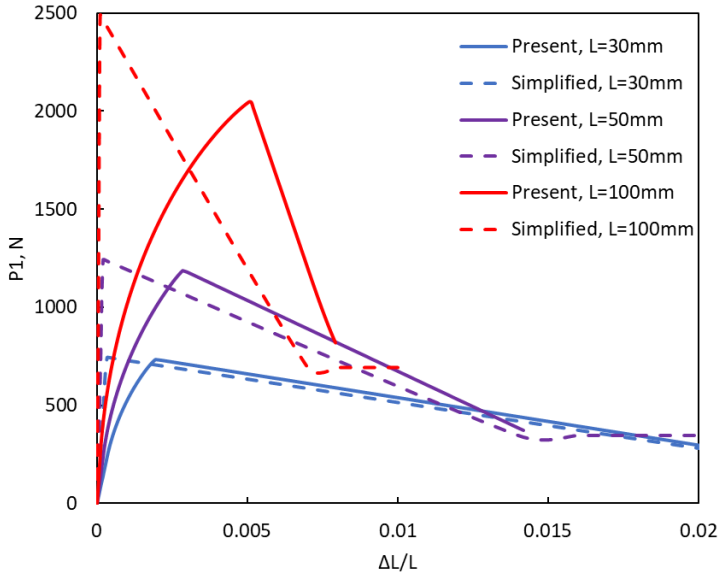

Figure 7 Load-displacement curves using both simplified and proposed methods ($\beta = 0, \eta = 0, \delta_1 = 0.01mm, \delta_2 = 0.7mm, \tau_f = 7.2MPa, and\ \tau_r = 2\ MPa$)

4.3. Effect of loading conditions on the concrete

4.3.1 Effect of pull-pull and pull-push loading conditions in a pull-out test

The pull-out test has been widely used to experimentally investigate the interfacial bond performance. However, there has not been a standard pull-out testing method for textile reinforced concrete due to large variation in textile reinforcement types and configurations [39]. For flexible impregnated textiles and dry textiles where the bond strength is rather weak, the double-sided pull-out test has been recommended [18], while for hard impregnation materials such as epoxy resin, the single sided pull-out test has been used [17]. The obvious difference between the two types of pull-out test setups is the loading condition for concrete matrix (as shown in Figure 8). The double-sided pull-out test follows the concept of the conventional steel rebar reinforced concrete, where both the reinforcement and the concrete are loaded from one end. In this case, the reinforcement is loaded under tension, while concrete is under compression. However, the single-sided pull-out test follows a pull-pull loading condition, where the loads are applied from both ends, and both the reinforcement and the concrete are under tension. Figure 9 presents the full-range load-displacement curves for a pull-out test under both pull-pull ($\beta = 0, \eta = 0$) and pull-push ($\beta = 0, \eta = 1$) loading conditions. The analytical model in this paper provides very close bond behaviour predictions under the two different loading conditions, although the difference becomes more obvious with an increase in the bond length. However, the interfacial shear stresses and axial stresses in the reinforcement and concrete are significantly different, as shown in Figure 10-12. The corresponding locations on the load-slip curve are marked in Figure 9(b): the 'Elastic' stresses are plotted at the end of the 'Elastic' stage; the 'E-S' is plotted when slip ΔL is 0.1mm; the 'E-S-D' results follow up when slip ΔL=0.8mm; the 'S-D' results are at the end of the load-slip curve. As concrete is much weaker in tension than that in compression, it is impossible to resist a high tensile stress (for example, over 5MPa) for plane concrete (Figure 11(a)). Thus, the theoretical solution given in the present paper may overestimate the interfacial performance under pull-pull loading condition. A recent study carried out by Dalalbashi et al. [39] has experimentally compared the pull-out responses of different test set-up and found that pull-pull

load condition (slightly different from the setup in this paper) provides higher peak load and lower stiffness than the pull-push loading condition. This implies the importance of loading conditions for bond behaviour tests. Further research may be needed to fully understand this effect.

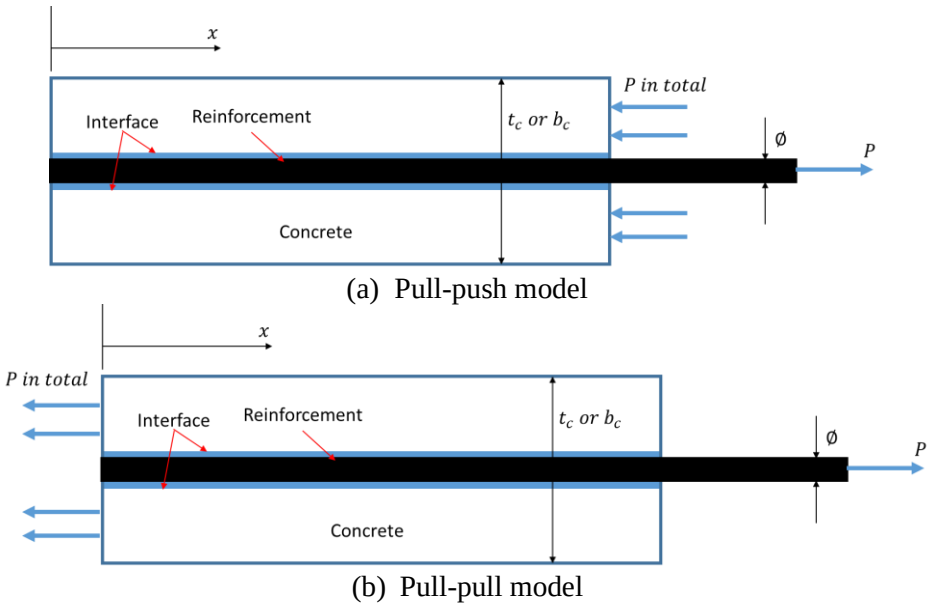

(a) Pull-push model

(b) Pull-pull model

Figure 8 Idealized illustrations of the pull-out test setup

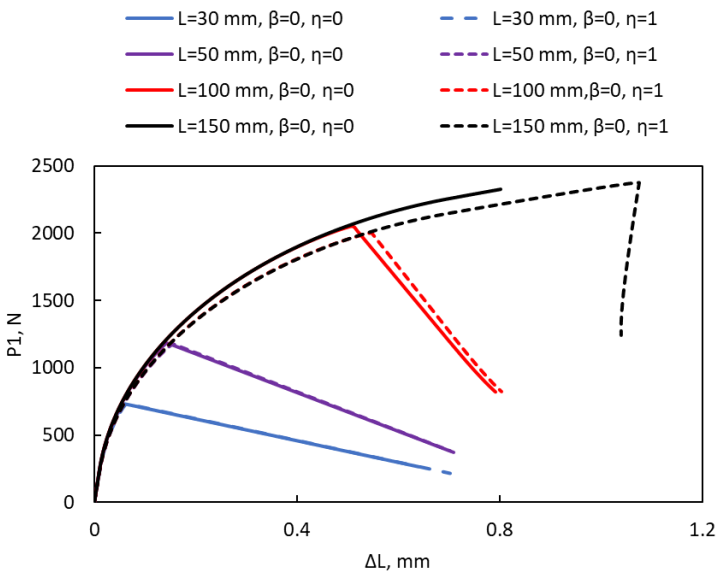

(a) Effect of bonding length

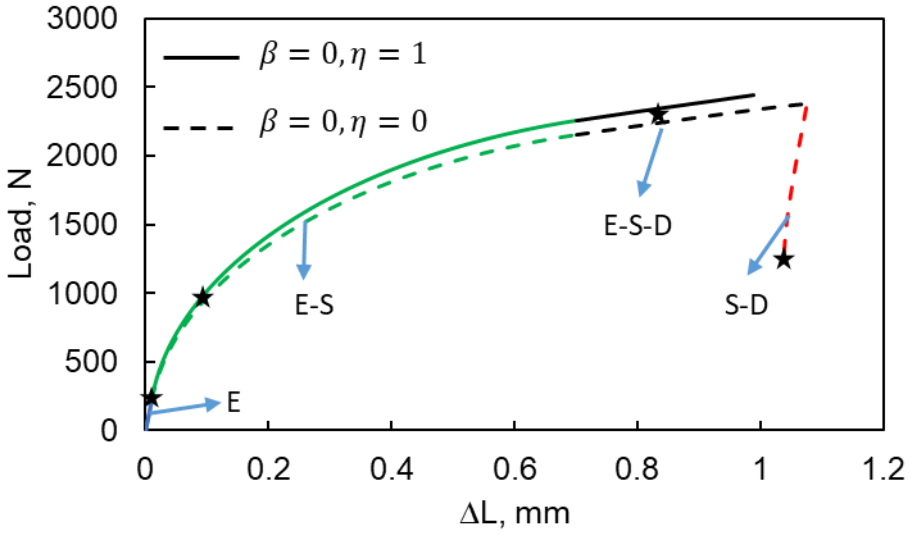

(b) Interfacial stages (L=150 mm)

Figure 9 Full-range load-displacement curves under different loading conditions ($\delta_1 = 0.01mm, \delta_2 = 0.7mm, \tau_f = 7.2MPa, and\ \tau_r = 2\ MPa$)

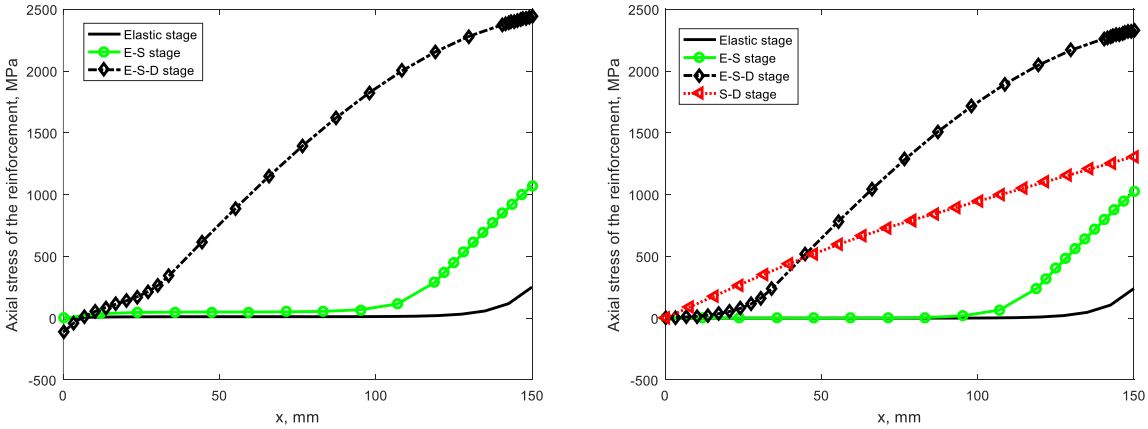

(a) Pull-pull loading ($\beta = 0, \eta = 0$) (b) Pull-push loading ($\beta = 0, \eta = 1$)

Figure 10 Axial stress distributions of reinforcement (L=150mm)

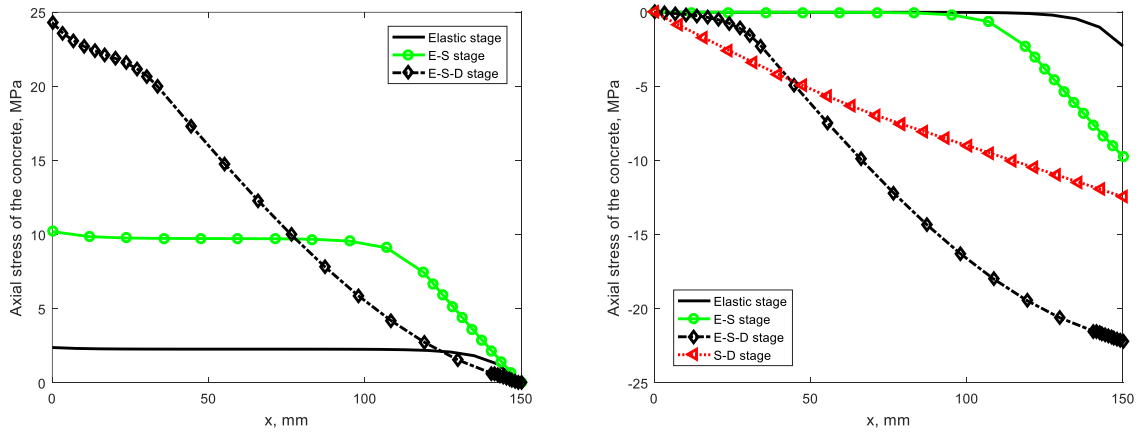

(a) Pull-pull loading ($\beta = 0, \eta = 0$) (b) Pull-push loading ($\beta = 0, \eta = 1$)

Figure 11 Axial stress distributions of concrete (L=150mm)

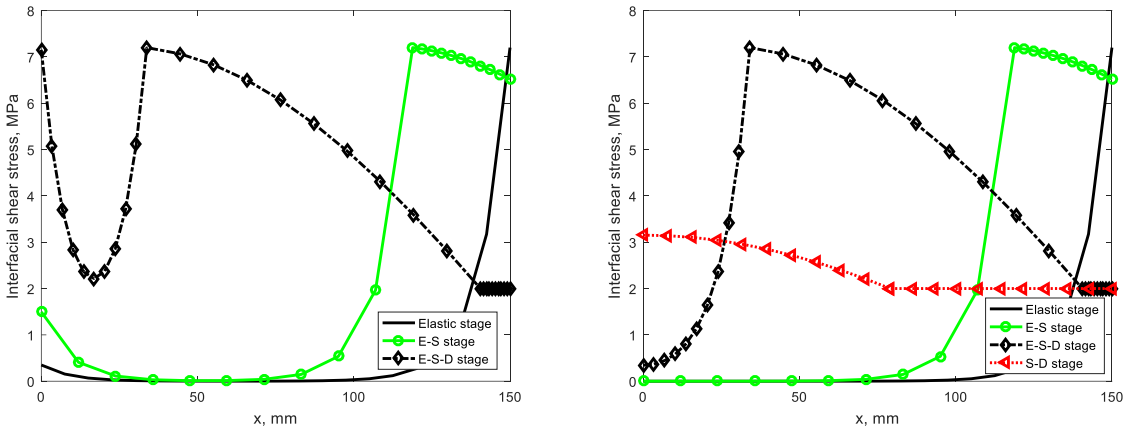

(a) Pull-pull loading ($\beta = 0, \eta = 0$) (b) Pull-push loading ($\beta = 0, \eta = 1$)

Figure 12 Interfacial shear stress distributions (L=150mm)

4.3.2 Effect of different β

Figure 13 shows the load-displacement relationship of a model with different β values, where the value of $\eta = 0$ (zero force on the right end of the matrix, i.e. cracked location), the bond length is taken as $L = 50mm$, and the reinforcement ratio is 1%. β value indicates different shear forces along the interface: $\beta = 0$ represents zero axial force at the left end of the reinforcement, i.e. interfacial shear force equals P_1, and $\beta = 1$ means equivalent axial forces at the two ends of the reinforcement, i.e. zero interfacial shear force. As $\beta = 1$ and $\eta = 0$ represents a pure bending loading condition, where the interfacial debonding does not occur [27], it is not included in this analysis. Figure 13 shows that, with the increase of β value, the ultimate load capacity of the model continues to increase, indicating debonding failure is less likely for a high β value. Assume the fibre breaking strength is 1.5GPa, the horizontal black dashed lines in Figure 13 indicate the fibre breaking force, i.e. axial force higher than that would not be possible to be carried by the reinforcement. Therefore, for the given length of 50mm in this example, the model will not fail by debonding if β value is larger than 0.3.

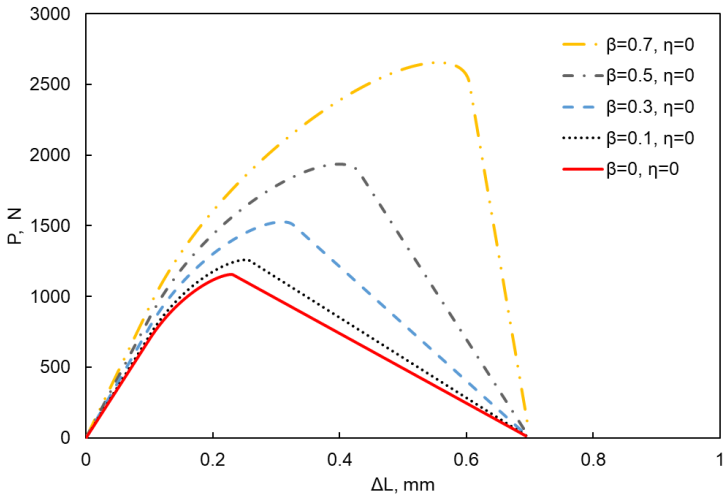

(a) $\tau_r = 0MPa$

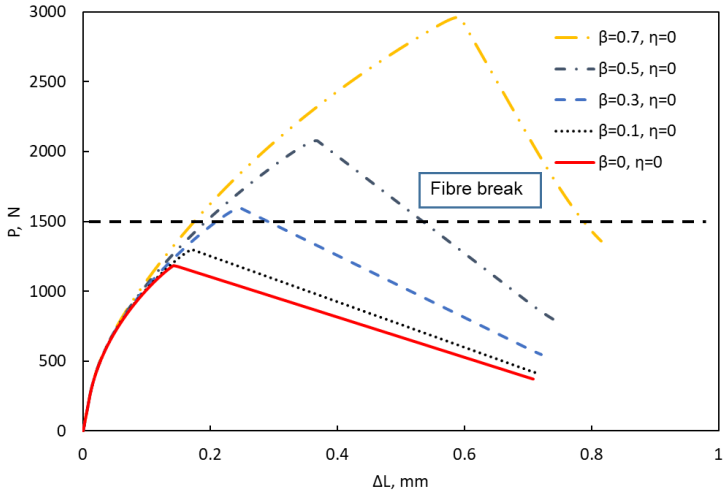

(b) $\tau_r = 2MPa$

Figure 13 Full-range load-displacement curves with various β (L=50mm)

4.3.3 Effect of different η

One case study of various η values is the crack development in a fibre reinforced concrete, as illustrated in Figure 14. Short fibres, such as steel fibre, carbon fibre, glass fibre or PVA fibre, are commonly used in concrete to control crack propagation. Once the concrete has cracked in the tension zone, instead of breaking completely, the small short fibres continue to 'glue' the concrete together by crack bridging. The effect of the short fibres could be assessed by using different η values in the analytical method proposed in this paper, and the effectiveness of crack control can be evaluated through the relative slip ΔL. Figure 15 shows the load-displacement relationship for different η values, with $\beta = 0.5$. The bond length is taken as $L = 50mm$, and the reinforcement ratio is 1%. Figure 15 indicates that, the ultimate bond load could be doubled if the short fibres could share half of the tensile load on the cracked section (e.g. $\eta = -1$). The increase of the ultimate load is almost proportional to the load capacity of the short fibres. Moreover, the control of the crack width is even more effective with the increase of η values. Taking a 1kN load as a reference (green flat dashed line in Fig. 15), the relative slip ΔL (an indicator of the crack width) when $\eta = -1$ is only 26.8% of the slip when $\eta = 0$. Note that the results shown in Figure 15 are only conceptual, as they are based on idealised conditions, where the introduction of micro fibres will not weaken the interfacial properties between the reinforcement and the matrix. Further experimental studies are needed to validate the findings.

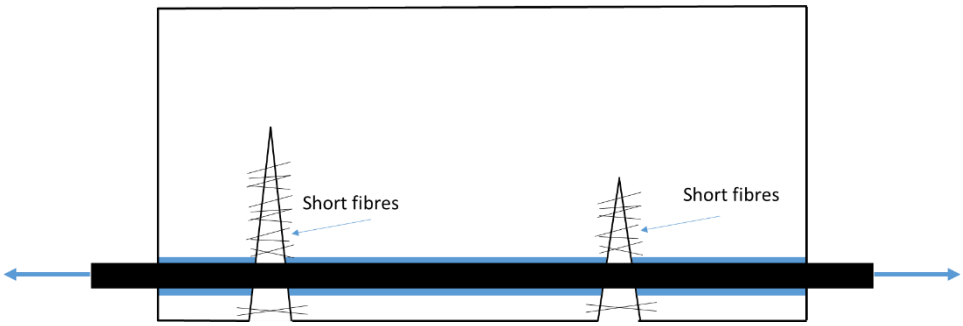

Figure 14 Crack development and control mechanism of a fibre-reinforced concrete

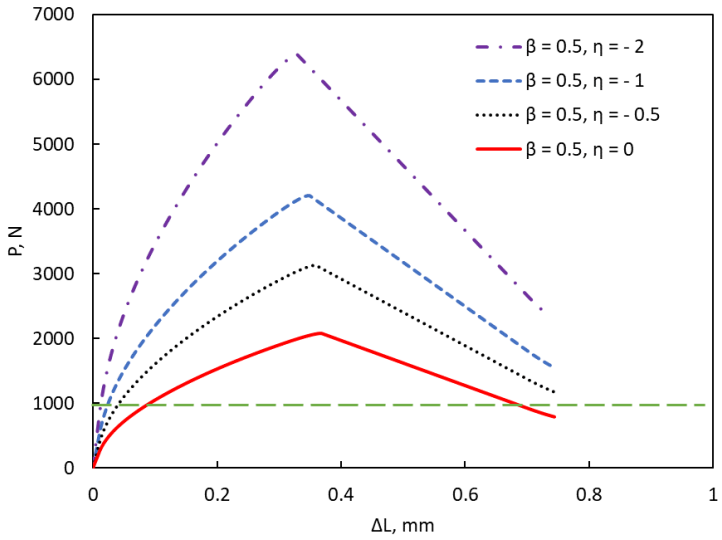

Figure 15 Full-range load-displacement curves with various η (L=50mm)

4.4. Effect of bond length

4.4.1 Effect of bond length under pull-out load conditions

Figure 16 shows load-displacement curves of pull-out samples with various bonding lengths under pull-push load conditions ($\beta = 0, \eta = 1$). The concrete has a width of 10mm and depth of 10mm, representing a reinforcement ratio of 1%. It is found that bond length does not affect the initial load-slip behaviour of the interface. However, when the bond length is too small, the model is not able to develop full bond-slip behaviour, as the interface fails in the elastic or softening range. This is demonstrated by plotting the interfacial shear stress distributions shown in Figure 17.

If the residual shear stress τ_r is zero, there exists an effective bond length [27], where the ultimate load does not increase further with an increase of the bond length, i.e.

$$L_e \approx 1.2a_u \tag{128}$$

in which a_u is the critical bond length for a fully developed softening distance [27]. a_u is equivalent to L_{cr} as presented in Eq. (114).

However, if the frictional residual shear stress is not zero, the ultimate load continues to increase with the increase of the bond length. To an extent the ultimate load could even exceed the material strength of reinforcement and concrete, indicating that the debonding will not be a critical failure mode. In terms of an initial and conservative estimation of the effective bond length, Eq. (128) may be acceptable for the cases with nonzero residual shear stresses.

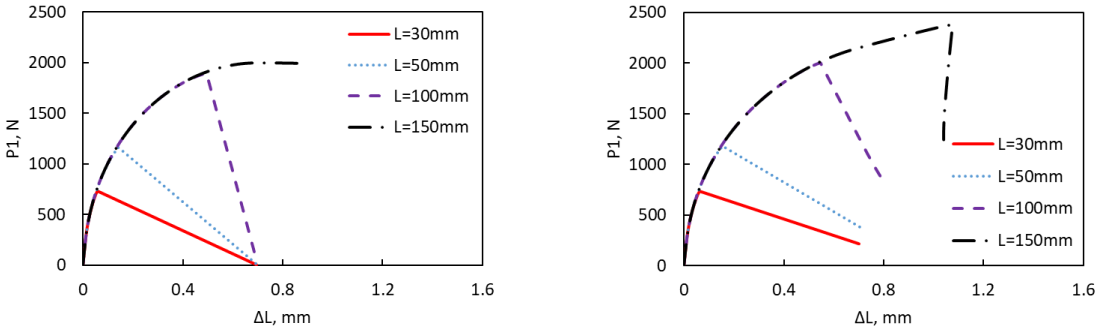

(a) $\beta = 0, \eta = 1, \tau_r = 0\ MPa$ (b) $\beta = 0, \eta = 1, \tau_r = 2\ MPa$

Figure 16 Full-range load-displacement curves using local bond-slip law in paper [1]

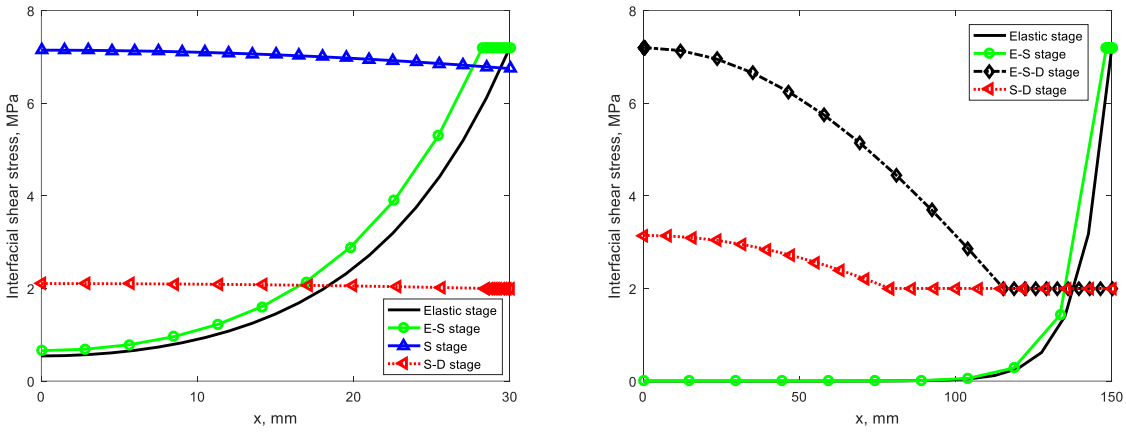

(a) $L = 30mm$ (b) $L = 150mm$

Figure 17 Interfacial shear stress distributions ($\beta = 0, \eta = 1, \tau_r = 2\ MPa$)

4.4.2 Effect of bond length of uncracked-cracked samples

Crack spacing is a key parameter to be investigated for a reinforced concrete structure, which reflects the strain hardening and ductility performance. Although the present method is based on simplified 1D model, which could not precisely predict crack initiation and propagation, it could be used to estimate minimum crack spacing of the specimen. Figure 18 shows the relation of bond length vs. ultimate load of uncracked-cracked samples considering two different reinforcement ratio (α=0.5% and α=2%), and two different bond strength ($\tau_f = 5MPa$ and $\tau_f = 7.2MPa$). On the cracked side (Side B, $\eta = 0$), all axial force is carried by the fibre reinforcement (P_1); while on the uncracked side (Side A), concrete matrix and fibre reinforcement deform uniformly, so P_2 and P_4 together counteract P_1. Based on the condition that the strain in the reinforcement and the concrete are equal on the uncracked side, β (= P_2/P_1) is obtained as:

$$\beta = \frac{(1-\eta)E_1A_1}{E_2A_2 - E_1A_1} \tag{129}$$

Figure 18(b) shows the trend of the ultimate load of a specimen with the increase of the bond length. It is found that the relation is close to linearity. This may be true when the bond length is significantly smaller than the critical bond length L_{cr} (=103.5mm in the case of α=2%). This indicates that the elastic limit load $P_{1,elastic\ limit}$ (Eq. (35)) may be valid to predict the ultimate load capacity of an uncracked-cracked tensile sample:

$$P_{1,pred} = P_{1,elastic\ limit,L=1mm} * L \tag{130}$$

A trend line (red dotted line) has been illustrated in Figure 18(b) for the specimen of α=2%, $\tau_f = 7.2MPa$. The error is found to be increasing with the increase of the bond length, and a difference of 10% is found for a bond length of 60mm. Assume that the fibre has a breaking strength of 1.5GPa, and concrete has a tensile strength of 5MPa, the dashed lines in Figure 18(b) indicate failure of fibre strand and concrete matrix specifically. In the case of α=2% and $\tau_f = 7.2MPa$, it is found that the specimen will fail by debonding if the bond length is smaller than 10mm. When the bond length is larger than 10mm, concrete matrix will exceed its tensile strength on the left end, indicating an initiation of a new crack. Similarly, in the case of α=0.5%, a new crack will generate when the bond length is larger than 30mm. Comparing the two cases, it is found that a higher reinforcement ratio (α=2%) reflects a potential of generating more cracks, thus better strain hardening performance and better ductility. Comparing the two cases of different bond strength, it is found that the case of $\tau_f = 5MPa$ would require a minimum bond length of 60mm to generate a new crack, which is double the bond length of the case of

$\tau_f = 7.2MPa$. Findings can be that lower bond strength (i.e. weaker interfacial properties) could lead to poor strain hardening performance, by worsening the crack development capability.

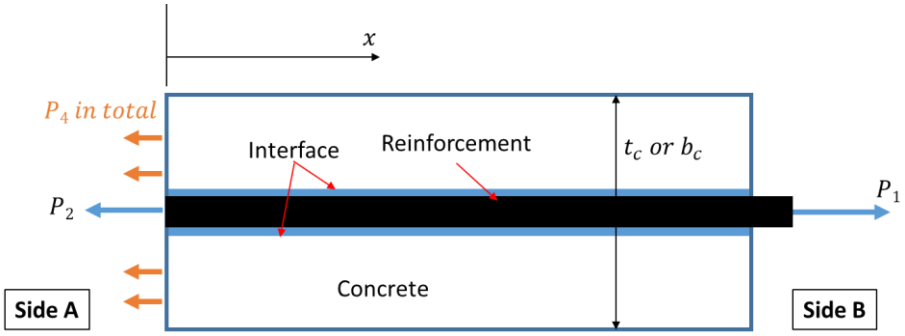

(a) Sketch of an uncracked-cracked specimen

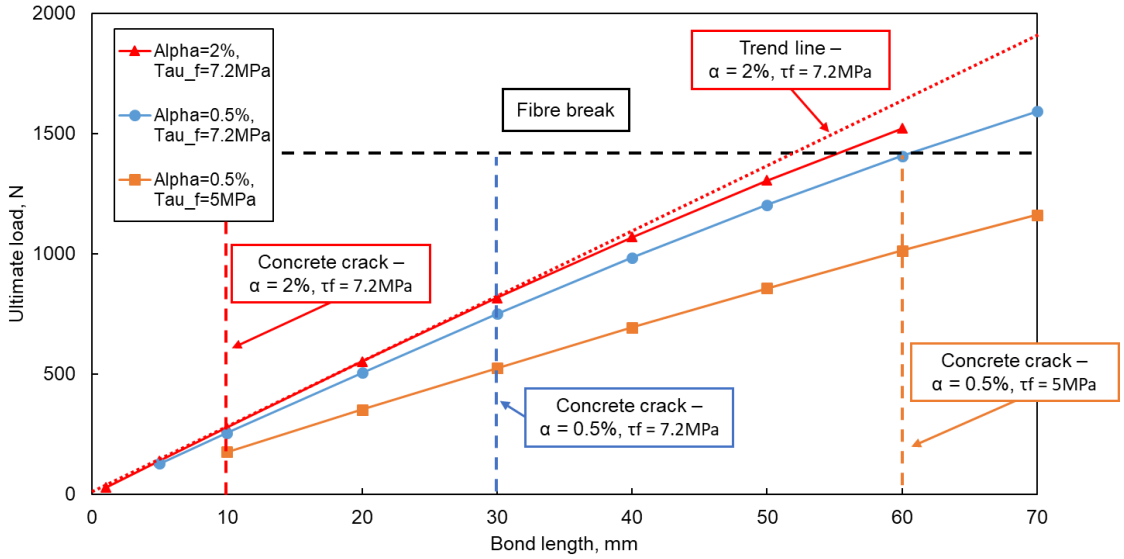

(b) Bond length – ultimate load relationship of uncracked-cracked specimens

Figure 18 Bond length – ultimate load relationship

4.5. Effect of frictional shear stress

Figure 19 compares the load-displacement curves of models with different bond lengths and frictional shear stresses. $\beta = 0, \eta = 0$ (pull-pull loading condition) and a reinforcement ratio of 1% were adopted. As shown in the figure, the ultimate load increases with the increase of the bond length, until the bond length is sufficiently large (e.g. $\frac{L}{A} \geq 100$ in this paper). If the friction over the debonded length is ignored ($\tau_r = 0$), the interface has a maximum bond load, where the ultimate load does not increase irrespective of the increase in bond length. However, in the cases where the reinforcement is embedded in the concrete, a certain friction exists on the debonded interface. In the case of a frictional shear stress of $\tau_r = 2\ MPa$, the ultimate load continues to increase after debonding. Thus the mechanical friction caused by aggregate interlocking plays a role in the bond hardening behaviour. Surface treatment of carbon fibre textiles (sticking sand) is an example of improving mechanical bonding of textile reinforced concrete. However, if the fibre breaking strength is taking into consideration (horizontal dashed line in Figure 19), it is seen that the effect of frictional shear stress may be minimal in the loading stage.

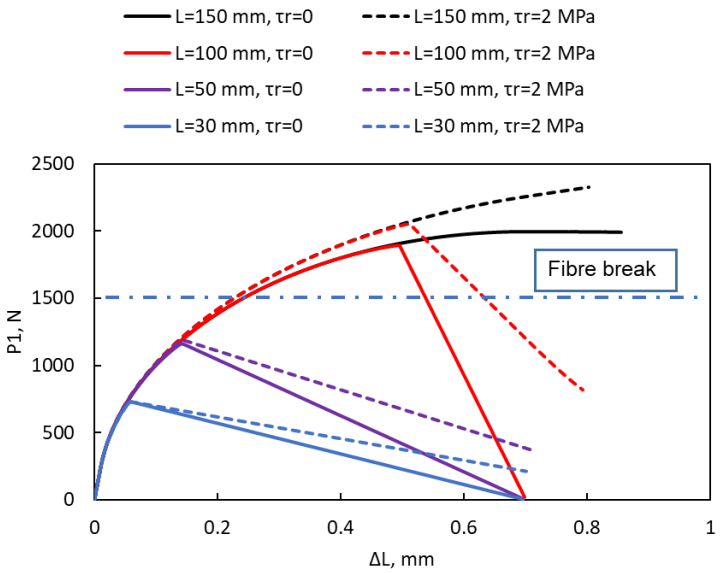

Figure 19 Load-displacement relation: effect of frictional shear stresses

4.6. Effect of reinforcement ratio

Figure 20 shows the load-displacement relationship at the right end of a model under pull-pull loading condition. Three different reinforcement ratios α have been adopted. It is found that the interfacial behaviour does not vary much if neglecting the material failure, i.e. the mechanical properties of both the fibre and the concrete matrix are assumed perfectly elastic. However, if taking into consideration the low tensile strength (e.g. 5MPa) of the concrete matrix, the axial stress of concrete has far exceeded its tensile yield strength during debonding (as shown in Figure 21). The ultimate load could only reach 350N for a bond length of 30mm, and a reinforcement ratio of 2% (Figure 20(b)). Therefore, for textile reinforced concrete with a high level of reinforcement (e.g. pultruded members), in order to make good use of the high tensile strength of the carbon fibres, it is essential to improve the tensile strength capacity of the concrete matrix. It may be necessary to use either the ultra-high strength concrete or short/micro fibre reinforced concrete.

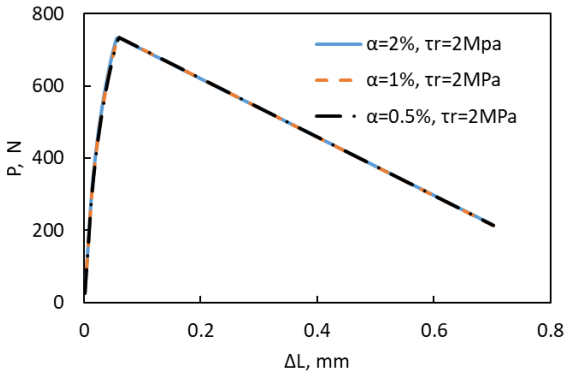

(a) $L = 30\ mm$, ignore material failure

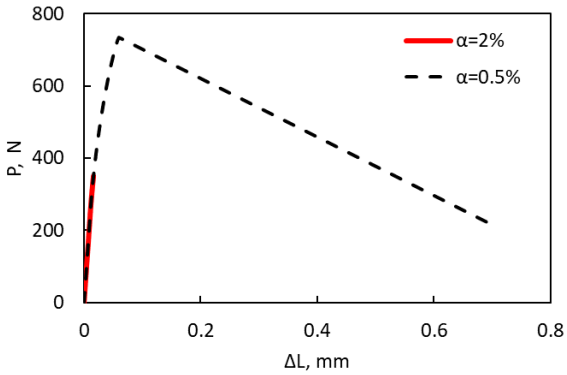

(b) $L = 30\ mm$, consider material failure

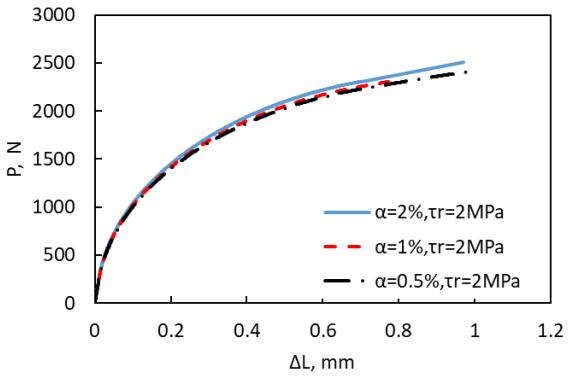

(c) $L = 150\ mm$, ignore material failure

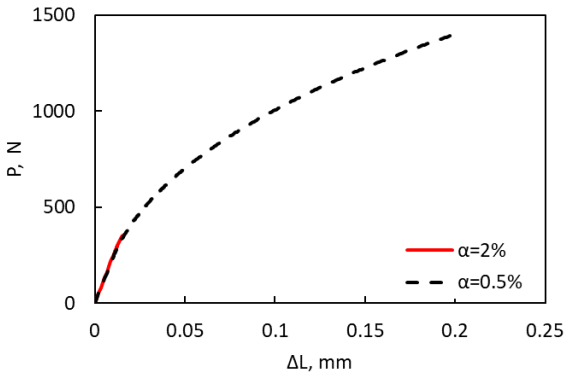

(d) $L = 150\ mm$, consider material failure

Figure 20 Load-displacement curves with different reinforcement ratios

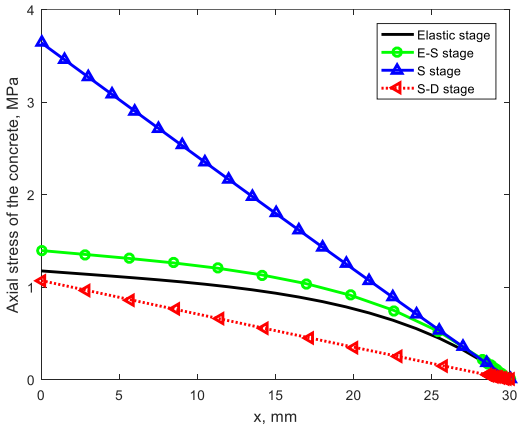

(a) $L = 30\ mm, \alpha = 0.5\%, \tau_r = 2\ MPa$

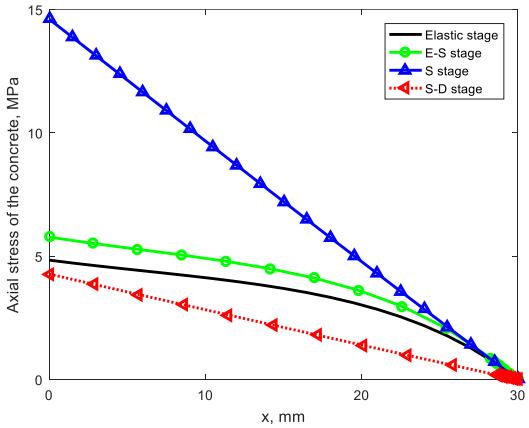

(b) $L = 30\ mm, \alpha = 2\%, \tau_r = 2\ MPa$

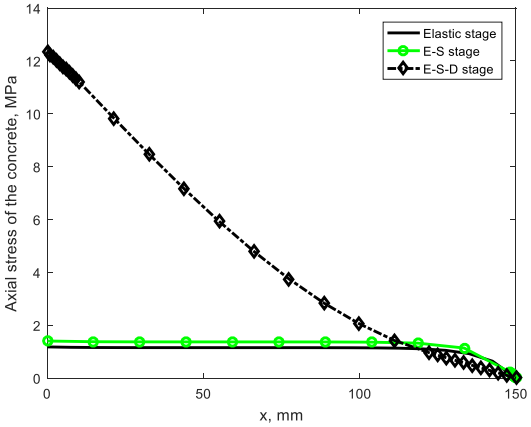

(c) $L = 150\ mm, \alpha = 0.5\%, \tau_r = 2\ MPa$

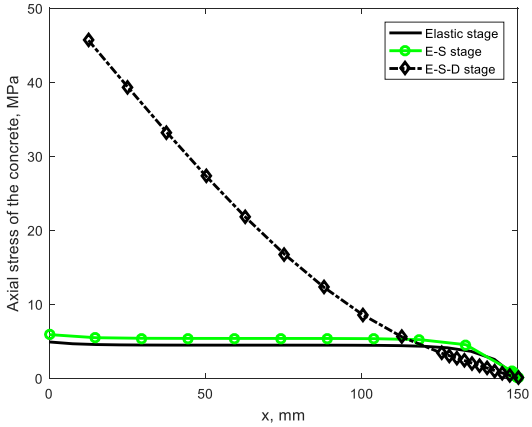

(d) $L = 150\ mm, \alpha = 2\%, \tau_r = 2\ MPa$

Figure 21 Axial stress distributions of the concrete at various stages during debonding

5. Conclusions

This paper has presented a closed-form solution for a bond-slip model of a textile reinforced concrete in the region between two cracks. The analytical solution enables the prediction of the full debonding propagation process, including the interfacial shear stress distributions and axial stresses in the reinforcement and the matrix. This will assist in understanding the mechanical

behaviour of the textile-to-concrete interface and help in optimizing the structural design of textile reinforced concrete. Note that the analytical solution is based on the assumptions that the geometry is uniform along the bond length, and that the material response is elastic throughout the loading process, the analytical model provides an upper bound of the load-slip behaviour. Based on the parametric studies in this paper, the following conclusions can be drawn:

(1) The simplified approach of evaluating local bond-slip relation via a pull-out test, with the assumption of uniform interfacial shear stress along the bond length, is not reliable in textile reinforced concrete, due to the large variation of the relative slip distributions along the interface. In general, the simplified method underestimates both the bond strength and the maximum relative slip at the interface.

(2) If the residual shear stress (friction after debonding) is neglected, there exists an effective bond length, beyond which the ultimate load does not increase with increase in the bond length. However, if the residual shear stress is taken into account, there is no ultimate load for debonding failure. For an initial estimation, the effective bond length of $1.2L_{cr}$ may be adopted for cases of nonzero residual shear stresses.

(3) The two different possible arrangements for pull-out tests in textile reinforced concrete, i.e. the pull-pull load condition and the pull-push load condition, do not significantly affect the load-slip relationship in the specimen if the materials are elastic throughout the loading process. However, taking into account the weak tensile strength of the concrete, the pull-pull test setup may not be able to predict the full-range load-slip relation for a long bond length.

(4) The ultimate debonding load increases substantially with an increase in the β value, indicating that debonding may not be the dominant failure mode for a model with a large β value.

(5) The load-slip relation is also significantly affected by the η values, indicating that using micro/short fibres in the concrete matrix will significantly improve the bond performance. For example, if the short fibres on a cracked section could resist half of the total tensile load, the ultimate debonding load could be doubled, and the crack width could be reduced to 26.8% compared with the case with no short fibres.

(6) Reinforcement ratio and the maximum interfacial shear strength have significant influence on the minimum crack spacing in a tensile member. The higher the reinforcement ratio, the smaller the minimum crack spacing, and thus the better strain hardening behaviour. However, this is based on the assumption that the local bond-slip relation won't be affected by the reinforcement ratio.

(7) Considering the weak tensile strength of the concrete, a high reinforcement ratio may alter the critical failure mode from debonding, to failure of the concrete matrix in textile reinforced concretes. Therefore, for textile reinforced concrete with a high level of reinforcement (e.g. pultruded members), it may be necessary to use either the ultra-high strength concrete or short/micro fibre reinforced concrete.

6. References

[1] Al-Gemeel, A. N., & Zhuge, Y. (2019). Using textile reinforced engineered cementitious composite for concrete columns confinement. Composite Structures, 210, 695-706.

[2] Irshidat, M. R., & Al-Shannaq, A. (2018). Using textile reinforced mortar modified with carbon nano tubes to improve flexural performance of RC beams. Composite Structures, 200, 127-134.

[3] Sharei, E., Scholzen, A., Hegger, J., & Chudoba, R. (2017). Structural behavior of a lightweight, textile-reinforced concrete barrel vault shell. Composite Structures, 171, 505-514.

[4] Portal, N.W., Perez, I.F., Thrane, L.N., and Lundgren, K. (2014). Pull-out of textile reinforcement in concrete. Construction and Building Materials, 63-71.
[5] Hegger, J., Goralski, C., Kulas, C. (2011). A pedestrian bridge made of textile reinforced concrete. Schlanke Fußgängerbrücke aus Textilbeton, 106 (2), 64-71.
[6] Zhu, J.-h., Su, M.-n., Huang, J.-y., Ueda, T., & Xing, F. (2018). The ICCP-SS technique for retrofitting reinforced concrete compressive members subjected to corrosion. Construction and Building Materials, 167, 669-679.
[7] Si Larbi, A., Contamine, R., Ferrier, E., & Hamelin, P. (2010). Shear strengthening of RC beams with textile reinforced concrete (TRC) plate. Construction and Building Materials, 24(10), 1928-1936.
[8] Brameshuber W. (2014) Test methods and design of Textile Reinforced Concrete. Report of RILEM TC 232-TDT. RILEM publications.
[9] Deluce, J.R., Vecchio, F.J. (2013). Cracking Behaviour of Steel Fibre-reinforced Concrete Members Containing Conventional Reinforcement. ACI Structural Journal, 110(3), 481-490.
[10] Banholzer, B., Brameshuber, W., Jung, W. (2006) Analytical evaluation of pull-out tests - the inverse problem. Cement Concrete Composites, 28 (6), 564-571.
[11] Xu, S., Li, H. (2007). Bond properties and experimental methods of textile reinforced concrete. Journal of Wuhan University of Technology-Mater. Sci. Ed., 22(3), 529-532.
[12] Sueki, S., Soranakom, C., Mobasher, B., Peled, A. (2007). Pull out-slip response of fabrics embedded in a cement paste matrix. J Mater Civ Eng, 19 (9), 718-727.
[13] Lorenz, E., Ortlepp, R. (2012). Bond behavior of textile reinforcements-development of a pull-out test and modeling of the respective bond versus slip relation. High performance fiber reinforced cement composites, 6, 479-486.
[14] Bielak, J., Li, Y., Hegger, J., Chudoba, R. (2018). Characterization procedure for bond, anchorage and strain-hardening behaviour of textile-reinforced cementitious composites, ICEM Proceedings, 2, 395. Doi: 10.3390/ICEM18-05224.
[15] Lorenz, E., Schütze, E., Weiland, S. (2015). Textilbeton–eigenschaften des verbundwerkstoffs, Bet Stahlbetonbau, 110 (S1), pp. 29-41.
[16] Abdullah, F. Textile Reinforced Concrete: Design Methodology and Novel Reinforcement. PhD thesis 2015, University of Leeds.
[17] Focacci, F., Nanni, A., and Bakis, C.E. Local bond-slip relationship for FRP reinforcement in concrete. ASCE Journal of Composites for Construction, 2000:24-31.
[18] Li, Y. , Bielak, J. , Hegger J., and Chudoba, R. An incremental inverse analysis procedure for identification of bond-slip laws in composites applied to textile reinforced concrete. Composites Part B: Engineering, 2018: 111-122.
[19] Wozniak, M., Tysmans, T., Verbruggen, S., Vantomme, J. (2017) Nonlinear indirect identification method for cement composite-to-concrete bond, Compos Struct, 176, 72-81.
[20] Focacci, F., Nanni, A., Bakis, C.E. (2000) Local bond-slip relationship for frp reinforcement in concrete, J Compos Constr, 4 (1), 24-31.
[21] Ferreira, S.R., Martinelli, E., Pepe, M., de Andrade Silva, F., Toledo Filho, R.D. (2016) Inverse identification of the bond behavior for jute fibers in cementitious matrix, Compos Part B Eng, 95, 440-452.
[22] R. Oliveira, M. Ramalho, M. Corrêa. A layered finite element for reinforced concrete beams with bond–slip effects, Cem Concr Compos, 30 (3) (2008), pp. 245-252
[23] I. Vilanova, L. Torres, M. Baena, M. Llorens Numerical simulation of bond-slip interface and tension stiffening in gfrp rc tensile elements, Compos Struct, 153 (2016), pp. 504-513
[24] Naaman, A.E., Namur, G.G., Alwan, J.M., Najm, H.S. (1991). Fiber pullout and bond slip. i: analytical study, J Struct Eng, 117 (9), 2769-2790.

[25] Dai, J., Ueda, T., Sato, Y. (2005) Development of the nonlinear bond stress–slip model of fiber reinforced plastics sheet–concrete interfaces with a simple method, J Compos Constr, 9 (1), 52-62.
[26] Yuan, H., Teng, J.G., Seracino, R., Wu, Z.S., and Yao, J. (2004) Full-range behavior of FRP-to-concrete bonded joints. Engineering Structures, 26(5), 553-565.
[27] Teng, J.G., Yuan, H., Chen, J.F. (2006) FRP-to-concrete interfaces between two adjacent cracks: Theoretical model for debonding failure. International Journal of Solids and Structures, (43), 5750-5778.
[28] Liu, S., Yuan, H., Wu, J. (2018) Full-range mechanical behavior study of FRP-to-concrete interface for pull-pull bonded joints. Composites Part B, 164,333-344.
[29] Lin, X., Zhang, Y.X. Evaluation of bond stress-slip models for FRP reinforcing bars in concrete. Composite Structures, 2014:131-141.
[30] Matlab. The MathWorks. https://uk.mathworks.com/products/matlab.html
[31] ANSYS. https://www.ansys.com/
[32] Banholzer, B. Bond of a strand in a cementitious matrix. Materials and structures, 39(10) 2006: 1015-1028.
[33] Cheng, S. Mechanical behaviour of fibre-to-concrete interface in textile reinforced concrete: theoretical model. ASME 2018, Hong Kong.
[34] Peled, A. and A. Bentur. Fabric structure and its reinforcing efficiency in textile reinforced cement composites. Composites Part A: Applied Science and Manufacturing, 34(2) 2003: 107-118.
[35] Naaman, A.E., Namur, G.G., Alwan, J.M., Najm, H.S. (1991). Fiber pullout and bond slip. i: analytical study, J Struct Eng, 117 (9), 2769-2790.
[36] Naaman, A.E., Namur, G.G., Alwan, J.M., Najm, H.S. (1991). Fiber pullout and bond slip. ii: Experimental validation, J Struct Eng, 117 (9), 2791-2800.
[37] Sueki, S., Soranakom, C., Mobasher, B., Peled, A. (2007). Pull out-slip response of fabrics embedded in a cement paste matrix. J Mater Civ Eng, 19 (9), 718-727.
[38] Lorenz E., Ortlepp R. (2012) Bond behaviour of textile reinforcements - Development of a pull-out test and modelling of the respective bond versus slip relation. In: Parra-Montesinos G.J., Reinhardt H.W., Naaman A.E. (eds) High performance fiber reinforced cement composites 6. RILEM State of the Art Reports, vol 2. Springer, Dordrecht.
[39] Dalalbashi A, Ghiassi B, Oliveira D.V., Freitas A. (2018) Effect of test setup on the fiber-to-mortar pull-out response in TRM composites: Experimental and analytical modelling. Composites Part B: Engineering, 143, 250-268.
[40] Mesticou, Z., Bui, L., Junes, A., & Larbi, A. S. (2017). Experimental investigation of tensile fatigue behaviour of Textile-Reinforced Concrete (TRC): Effect of fatigue load and strain rate. Composite Structures, 160, 1136-1146.
[41] www.solutions-in-textile.com (accessed on 14th Nov 2019)
[42] Carozzi, F. G., Colombi, P., Fava, G., & Poggi, C. (2016). A cohesive interface crack model for the matrix–textile debonding in FRCM composites. Composite Structures, 143, 230-241.
[43] Yang, Y., Biscaia, H., Chastre, C., & Silva, M.A.G. (2017). Bond characteristics of CFRP-to-steel joints. Journal of Constructional Steel Research, 138, 401-419.
[44] Ren, F.F., Yang Z.J., Chen, J.F., & Chen, W.W. (2010). An analytical analysis of the full-range behaviour of grouted rockbolts based on a tri-linear bond-slip model. Construction and Building Materials, 24 (3), 361-370.
[45] Biscaia, H.C., Chastre C., Borba I.S., Silva C., & Cruz D. (2016). Experimental Evaluation of Bonding between CFRP Laminates and Different Structural Materials. ASCE Journal of Composites for Construction, 20 (3), doi: 10.1061/(ASCE)CC.1943-5614.0000631.

[46] D’Antino, T., Colombi, P., Carloni, C., Sneed, L.H. (2018). Estimation of a matrix-fiber interface cohesive material law in FRCM-concrete joints. Composite Structures, 193, 103-112.
[47] Calabrese, A. S., Colombi, P., & D'Antino, T. (2019). Analytical solution of the bond behavior of FRCM composites using a rigid-softening cohesive material law. Composites Part B: Engineering, 174, 107051.
[48] Colombi, P., & D'Antino, T. (2019). Analytical assessment of the stress-transfer mechanism in FRCM composites. Composite Structures, 220, 961-970.